bioRxiv preprint doi: https://doi.org/10.1101/2020.07.12.189621; this version posted July 12, 2020. The copyright holder for this preprint (which was not certified by peer review) is the author/funder. All rights reserved. No reuse allowed without permission.

TITLE

Wide phenotypic spectrum of human stem cell-derived excitatory neurons with Rett syndrome-associated *MECP2* mutations

AUTHORS

Rebecca SF Mok[1,2], Wenbo Zhang[3], Taimoor I Sheikh[4], Isabella R Fernandes[5], Leah C DeJong[1,2], Matthew R Hildebrandt[2], Marat Mufteev[1,2], Deivid C Rodrigues[2], Wei Wei[2], Alina Piekna[2], Jiaje Liu[2], Alysson R Muotri[5], John B Vincent[4], Michael W Salter[3], James Ellis[1,2]

[1]Department of Molecular Genetics, University of Toronto, Toronto, ON M5S 1A8, Canada.

[2]Developmental & Stem Cell Biology Program, The Hospital for Sick Children, Toronto, ON M5G 0A4, Canada.

[3]Neurosciences & Mental Health Program, The Hospital for Sick Children, Toronto, ON, Canada.

[4]Molecular Neuropsychiatry & Development (MiND) Lab, Campbell Family Mental Health Research Institute, Centre for Addiction and Mental Health, Toronto, ON M5T 1R8, Canada.

[5]University of California San Diego, School of Medicine, Department of Pediatrics/Rady Children's Hospital San Diego, Department of Cellular & Molecular Medicine, Stem Cell Program, La Jolla, CA 92037-0695, USA.

bioRxiv preprint doi: https://doi.org/10.1101/2020.07.12.189621; this version posted July 12, 2020. The copyright holder for this preprint (which was not certified by peer review) is the author/funder. All rights reserved. No reuse allowed without permission.

ABSTRACT

Rett syndrome (RTT) is a severe neurodevelopmental disorder primarily caused by heterozygous loss-of-function mutations in the X-linked gene methyl-CpG-binding protein 2 (*MECP2*) that is a global transcriptional regulator. Mutations in the methyl-binding domain (MBD) of MECP2 disrupt its interaction with methylated DNA required for proper function in the brain. Here, we investigate the effect of a novel MECP2 L124W missense mutation in the MBD in comparison to *MECP2* null mutations. L124W protein had a limited ability to disrupt heterochromatic chromocenters due to decreased binding dynamics. We isolated two pairs of isogenic WT and L124W induced pluripotent stem cell lines. L124W induced excitatory neurons expressed stable protein, exhibited only increased input resistance and impaired voltage-gated Na^+ and K^+ currents, and their neuronal dysmorphology was limited to reduced dendritic complexity. Three isogenic pairs of *MECP2* null neurons had the expected more pronounced morphological and electrophysiological phenotypes, exhibiting decreased soma area, dendrite length, capacitance and excitatory synaptic function. We examined development and maturation of excitatory neural networks using micro-electrode arrays to detect alterations in RTT connectivity. The L124W neurons had no detectable changes in network circuitry features, in contrast to *MECP2* null neurons that suffered a significant change in synchronous network burst frequency and a transient extension of network burst duration. Our results from stem cell-derived RTT excitatory neurons reveal a wide range of morphological, electrophysiological and circuitry phenotypes that reflect the severity of the *MECP2* mutation.

bioRxiv preprint doi: https://doi.org/10.1101/2020.07.12.189621; this version posted July 12, 2020. The copyright holder for this preprint (which was not certified by peer review) is the author/funder. All rights reserved. No reuse allowed without permission.

INTRODUCTION

Rett syndrome (RTT) is a rare neurodevelopmental disorder primarily affecting females and caused by heterozygous loss-of-function mutations in the gene methyl-CpG-binding protein 2 (*MECP2*) (Amir et al., 1999). RTT is characterized by early developmental regression leading to loss of language and motor skills, development of hand stereotypies, gait abnormalities, and in some cases autism-like behaviours, autonomic dysfunction and seizures (Chahrour and Zoghbi, 2007). *MECP2* is an X-linked gene that undergoes X chromosome inactivation (XCI) in female cells, resulting in mosaic expression of the WT and mutant *MECP2* alleles in RTT individuals that may alter symptom presentation in instances of non-random XCI (Archer et al., 2006; Knudsen et al., 2006). Although *MECP2* mRNA is ubiquitously expressed in all tissues, MECP2 protein is found to be most abundant in neurons (Shahbazian, 2002), where it binds methylated DNA as a global transcriptional regulator (Chahrour et al., 2008; Nan et al., 1997). A large number of RTT patient-associated *MECP2* missense mutations map to the methyl-binding domain (MDB) and disrupt the interaction with DNA required for proper MECP2 function (Tillotson and Bird, 2019).

Human stem cell-derived neuron models of RTT have been able to confirm many of the cellular phenotypes observed in *Mecp2* mouse models and RTT patients (Ananiev et al., 2011; Cheung et al., 2011; Djuric et al., 2015; Kim et al., 2011; Li et al., 2013; Marchetto et al., 2010; Mellios et al., 2018; Tang et al., 2019). In these studies, WT and *MECP2* point or null mutation embryonic or induced pluripotent stem cells (ESCs or iPSCs) were differentiated into neural precursor cells (NPCs) and then into electrically active cortical neurons. They showed that RTT neuron morphology and structure were affected when MECP2 was dysfunctional, exhibiting reduced soma area, dendrite length, branch complexity and number of excitatory synapses. When RTT neuron electrophysiology was investigated, they showed decreased action potential

bioRxiv preprint doi: https://doi.org/10.1101/2020.07.12.189621; this version posted July 12, 2020. The copyright holder for this preprint (which was not certified by peer review) is the author/funder. All rights reserved. No reuse allowed without permission.

numbers, fewer calcium transients and reduced frequency of spontaneous or mini excitatory post-synaptic currents (sEPSCs or mEPSCs). These studies consistently demonstrated that at the individual cell level, RTT neurons have decreased size and impaired excitatory neurotransmission, together suggesting a neuronal maturation defect.

It has been shown in electrophysiological studies of mouse cortical slices and hippocampal cultures that *Mecp2* neurons have decreased mEPSC frequency, while mini inhibitory post-synaptic current (mIPSC) properties remain largely unchanged (Dani et al., 2005; Nelson et al., 2006). This implied that decreased excitatory neuronal activity and alteration of activity-dependent gene expression regulated by MECP2 (Cohen et al., 2011) may alter circuit maturation dynamics and contribute to the observed RTT phenotypes. Recent approaches using induced excitatory neurons co-cultured with astrocytes on micro-electrode arrays (MEAs) now allow evaluation of the development of synchronous network activity and how that circuitry is affected by changes in genetic profiles that characterize neurodevelopmental disorders (Deneault et al., 2019; Frega et al., 2019; Nageshappa et al., 2016).

In this work, we investigate the impact of a novel *de novo* RTT patient-associated missense mutation in the MECP2 MBD at L124W (c.371T>G). This variant has unknown molecular consequences on MECP2 heterochromatin binding. We compared L124W to *MECP2* null excitatory neurons and their respective isogenic controls to define cellular consequences in neuron morphology and functional activity. We used MEAs to examine the development of synaptic connections during maturation to identify synchronous network bursting impairments in RTT excitatory neural cultures. Our results define a wide range of RTT-associated heterochromatin binding, neuron morphology, electrophysiology and circuitry phenotypes that can be modelled in human stem cell-derived neurons and correlate with the severity of *MECP2* mutation and clinical presentation.

bioRxiv preprint doi: https://doi.org/10.1101/2020.07.12.189621; this version posted July 12, 2020. The copyright holder for this preprint (which was not certified by peer review) is the author/funder. All rights reserved. No reuse allowed without permission.

RESULTS

Limited heterochromatin disruption by the MECP2 L124W protein

MECP2 is known to play a role in chromatin architecture (Georgel et al., 2003). The structure of crystallized human WT MECP2 MBD bound to the *BDNF* promoter (Ho et al., 2008) demonstrated that the location of L124 maps in close 3D proximity to R106 (Fig1A). According to RettBASE (Krishnaraj et al., 2017), a database of patient *MECP2* variants, both of these residues are mutated in classical Rett syndrome patients to L124F and R106W, respectively. When these two variants were expressed in mouse cells they disrupted heterochromatic chromocenters (Agarwal et al., 2011; Kudo, 2003; Sheikh et al., 2016). To investigate whether the novel L124W MBD missense mutation disrupts heterochromatin similarly to L124F and R106W, we assessed its ability to bind and cluster chromocenters. In brief, we overexpressed MECP2-GFP fusions in C2C12 mouse myoblast cells, which have low levels of endogenous Mecp2. GFP colocalization with DAPI marked chromocenters was measured by confocal microscopy. WT showed distinctly formed chromocenter clusters with high colocalization of GFP and DAPI as expected, while R106W and L124F showed completely disrupted chromocenter clustering and indistinct GFP and DAPI colocalization (Fig. 1B). In contrast, the novel L124W mutation showed limited heterochromatin disruption characterized by unaffected chromocenter number and reduced chromocenter size (Fig1B,C). L124W also was more distributed through the nucleus showing reduced colocalization of GFP with DAPI as measured by Pearson's correlation coefficient (PCC) (Fig 1B,C).

To further explore the binding dynamics of L124W protein, fluorescence recovery after photobleaching (FRAP) live-imaging was used to study MECP2 protein mobility (Sheikh et al., 2016). WT and L124W MECP2-GFP fusion proteins were overexpressed in C2C12 cells, and following photobleaching of a single chromocenter foci, MECP2-GFP fusion protein signal

bioRxiv preprint doi: https://doi.org/10.1101/2020.07.12.189621; this version posted July 12, 2020. The copyright holder for this preprint (which was not certified by peer review) is the author/funder. All rights reserved. No reuse allowed without permission.

recovered more rapidly in the L124W compared to the WT over time (Fig. 1D, arrowheads). L124W had a shorter half-life and larger available unbound mobile fraction to recover the bleached signal that suggests it has decreased binding dynamics with heterochromatin (Fig. 1E). Taken together with the partial impairments in chromocenter clustering, these results point towards a limited effect of L124W mutation on MECP2 chromocenter association due to decreased binding dynamics.

Generation of MECP2 L124W iPSCs and Ngn2-derived excitatory neurons

As differences in genetic background and modifier genes contribute to RTT phenotype severity (Buchovecky et al., 2013; Scala et al., 2007), disease modelling strategies using isogenic WT cells provide the most precise controls for comparing to affected cells. By taking advantage of XCI in female somatic cells or gene-editing, we and others have generated isogenic pairs of RTT stem cell lines. We chose well-characterized cells with pronounced phenotypes including *MECP2* null isogenic lines derived from a classical RTT delta3-4 patient (Cheung et al., 2011) and the *MECP2* null line derived by gene editing of the human ESC line WIBR3 (Li et al., 2013) (Fig. 1F). As described below, we first sought to investigate the downstream cellular and functional consequences of L124W in the context of XCI isogenic human stem cell-derived excitatory neurons. Subsequently, we generated a third *MECP2* null isogenic pair using gene editing of the PGPC14 healthy control line.

We generated iPSCs from an atypical RTT patient (CLT) harbouring a heterozygous *MECP2* c.371T>G variant resulting in the novel L124W amino acid change. iPSCs were reprogrammed from fibroblasts using Sendai virus. Expanded clones were assessed for XCI status using the androgen receptor (AR) endonuclease digestion assay to isolate isogenic lines fully skewed to either the WT or mutant *MECP2* allele on the active X chromosome (X_a) (Fig. 1G). Two lines of X_a WT (CLT C4 and C17) and two lines of X_a L124W (CLT C1 and C2) were obtained with normal 46XX karyotype (Fig. S1A). Cell lines were routinely tested and found to

bioRxiv preprint doi: https://doi.org/10.1101/2020.07.12.189621; this version posted July 12, 2020. The copyright holder for this preprint (which was not certified by peer review) is the author/funder. All rights reserved. No reuse allowed without permission.

be mycoplasma free. Restricted mRNA expression of the X_a allele was confirmed by cDNA sequencing across the L124W variant (Fig. 1H) and shown to not be subject to erosion of the inactive X chromosome (X_i) (Mekhoubad et al., 2012) over extended passage. The iPSC lines demonstrated pluripotency by positive staining for OCT4, NANOG, SSEA-4 and TRA-1-60 (Fig. S1B), spontaneous differentiation into the 3-germ layers (Fig. S1C) and pluripotent cell expression profiles determined by RNA-seq and Pluritest analysis (Müller et al., 2011) (Fig. S1D).

To examine L124W protein levels in excitatory cortical neurons we used a rapid induced *Neurogenin-2* (*Ngn2*) over-expression protocol (Deneault et al., 2018; Zhang et al., 2013) (Fig. S1E). In brief, WT and RTT iPSCs/ESCs were transduced with the Tet-inducible *Ngn2-puro* lentivirus vectors, over-expression was induced with doxycycline for 8 days and selected with puromycin, and dividing cells were eliminated with AraC prior to excitatory neuron maturation. As expected, MECP2 capillary-based protein detection of 6 week old *Ngn2* neuron extracts demonstrated absence of MECP2 protein in d3-4 and WIBR null lines, but similar levels of L124W protein compared to their respective isogenic WT lines (Fig. 1I). We conclude that L124W protein is stable and produced at a normal level.

While we proceeded to evaluate the CLT, d3-4 and WIBR3 neurons for neuronal activity as described in the next section, we used CRISPR/Cas9 gene editing to isolate a novel *MECP2* null line. We introduced indels into a previously described unaffected female PGPC14 iPSC line from the Personal Genome Project Canada (Hildebrandt et al., 2019). PGPC14 iPSCs were co-transfected with Cas9 and a gRNA specific for exon 3 of *MECP2*. Selected clones were screened for normal karyotype (Fig. S1F) and found to be positive for hallmark pluripotency markers (Fig. S1G). cDNA sequencing identified a 1 bp insertion (c.217_218insC) into *MECP2* exon 3 on the X_a (Fig. S1H) of the PGPC14 null line, resulting in a frameshift and premature

bioRxiv preprint doi: https://doi.org/10.1101/2020.07.12.189621; this version posted July 12, 2020. The copyright holder for this preprint (which was not certified by peer review) is the author/funder. All rights reserved. No reuse allowed without permission.

truncation of the protein (p.Val74CysfsTer16) before the MBD (Fig. 1F). Generation of *Ngn2* neurons and protein detection by immunocytochemistry (Fig. S1I), capillary (Fig. 1J) and conventional western blot (Fig. S1J) demonstrated that PGPC14 indel neurons were *MECP2* null, compared with d3-4 null samples generated from NPC derived neurons. The PGPC14 parental cells exhibit robust differentiation into many cell types, in contrast to the d3-4 lines, and were employed for subsequent neuron morphology and circuitry experiments.

RTT Ngn2 neurons exhibit alterations in intrinsic membrane properties and excitatory synaptic function

To validate *Ngn2*-derived excitatory neurons as an appropriate cellular model of RTT, we examined their electrophysiology and asked if we could detect RTT-associated phenotypes. We performed whole cell patch-clamp recordings to investigate the intrinsic membrane properties of 4-5 week old *Ngn2* neurons from isogenic d3-4 (n = 66 and 58 neurons) and WIBR3 (n = 42 and 55 neurons) lines co-cultured with mouse astrocytes. We looked for changes in intrinsic membrane properties as previously reported in mouse iPSC-derived neurons and human RTT neurons conventionally differentiated via a neural precursor cell (NPC) stage (Djuric et al., 2015; Farra et al., 2012). Indeed, *MECP2* null neurons exhibited depolarized resting membrane potential, higher input resistance and decreased cell capacitance (Fig. 2A-C), consistent with previous findings on RTT neuron passive membrane properties. We next assessed whether *MECP2* mutant neurons had alterations in active membrane properties, as previously reported in RTT neurons (Djuric et al., 2015; Farra et al., 2012). Voltage-gated Na^+ and K^+ currents, under voltage-clamp condition, were evoked by depolarizing voltage steps from the holding potential of -70 mV. We found that both of Na^+ and K^+ currents were significantly diminished in d3-4 and WIBR3 null neurons, compared to their respective isogenic WT (Fig. 2E). Given these alterations in the intrinsic membrane properties, *MECP2*-deficient neurons should have dysfunction in action potential firing. We therefore performed whole-cell current-

bioRxiv preprint doi: https://doi.org/10.1101/2020.07.12.189621; this version posted July 12, 2020. The copyright holder for this preprint (which was not certified by peer review) is the author/funder. All rights reserved. No reuse allowed without permission.

clamp recordings to investigate the properties of action potentials, which were elicited by injecting a series of current steps from -5 pA to 100 pA in both WT and *MECP2*-deficient neurons (Fig. 2D & S2A). Together, these findings indicate that *MECP2* mutation causes alterations in intrinsic membrane properties and deficiency in action potential firing, which may lead to a further influence on the functions of neuronal network. We next examined synaptic transmission by recording mEPSCs in 6 week old *Ngn2* WT and RTT neurons from d3-4 (n = 56 and 62) and WIBR3 (n = 58 and 44). We observed reduced AMPAR-mEPSC amplitude and frequency in the *MECP2* null neurons (Fig. 2F), consistent with previous reports of hypo-activity in RTT NPC-derived cortical neurons. Taken together, these data from a total of 441 neurons indicate that WT *Ngn2* neurons are active but have some different intrinsic property baselines compared to NPC-derived neurons. Importantly, the *MECP2* null neurons recapitulated known RTT-associated excitatory neurotransmission phenotypes.

Based on the limited disruption of heterochromatin binding by L124W MECP2 protein, we predicted that L124W *Ngn2* neurons may not fully recapitulate the *MECP2* null electrophysiological properties. For passive membrane properties, L124W (n = 99 and 100 neurons) exhibited increased input resistance, but in contrast to *MECP2* null neurons, did not show differences in resting membrane potential or cell capacitance (Fig. 2G-I). For active membrane properties, L124W neurons did not have changed evoked action potential numbers with similar amounts of injected current as the *MECP2* null neurons and unaltered AP properties, but did exhibit impaired evoked Na^+ and K^+ currents (Fig. 2J,K & S2B). Next, when examining excitatory neurotransmission in WT and L124W *Ngn2* neurons (n = 68 and 78), L124W showed a trend (p = 0.06) towards reduced AMPAR-mEPSC amplitude and frequency (Fig. 2L). Therefore, recordings of 345 WT and L124W *Ngn2* neurons demonstrate common RTT electrophysiological properties of increased input resistance and impaired evoked currents. In contrast, *MECP2* null neurons also exhibited resting membrane potential and capacitance

bioRxiv preprint doi: https://doi.org/10.1101/2020.07.12.189621; this version posted July 12, 2020. The copyright holder for this preprint (which was not certified by peer review) is the author/funder. All rights reserved. No reuse allowed without permission.

differences, and reduced action potential numbers. We found from a cumulative total of 786 neurons a less severe profile of intrinsic membrane properties and synaptic transmission alterations in L124W compared to *MECP2* null neurons, revealing that a range of mutation-dependent RTT phenotypes can be detected in this *Ngn2* neuron *in vitro* model.

Altered neuronal size and complexity in RTT Ngn2 neurons

Reduced size and complexity have been identified as prominent morphometric features of human NPC-derived cortical neurons (Cheung et al., 2011; Li et al., 2013; Marchetto et al., 2010). This leads to a smaller cell membrane surface area which is thought to contribute to the decreased cell capacitance of *MECP2* null neurons in patch-clamp electrophysiology. Consequently, the lack of change in cell capacitance of the L124W neurons may indicate that their surface area or overall size of soma and dendrites would be unaltered. To assess this, 6 week old *Ngn2* neurons were co-cultured on mouse astrocytes and sparsely labelled with GFP in 3-5 independent experiments. The fixed cover slips were stained for DAPI, GFP and MAP2, and images captured on a confocal microscope reveal similar cell densities for all genotypes (Fig 3A). Soma area and dendrite tracing was performed by two blinded individuals. As expected d3-4, WIBR and PGPC14 *MECP2* null neurons had decreased soma area and total dendrite length, recapitulating the known RTT-associated phenotypes (Fig. 3B,C). In contrast, the L124W missense neurons exhibited no changes in soma area or dendrite length (Fig.3 B,C). Interestingly however, Sholl analysis of the L124W neurons did reveal a branching complexity deficit similar to the *MECP2* null neurons (Fig. 3D & S2A-B). Taken together from a total of 404 neurons, only the less complex morphology change displayed by the L124W missense mutation is shared with *MECP2* null neurons, consistent with more limited mutation-dependent phenotypes found in L124W protein heterochromatin association and excitatory neuron activity.

Aberrant network circuitry in MECP2 null Ngn2 neural cultures

bioRxiv preprint doi: https://doi.org/10.1101/2020.07.12.189621; this version posted July 12, 2020. The copyright holder for this preprint (which was not certified by peer review) is the author/funder. All rights reserved. No reuse allowed without permission.

Upon observing alterations action potential firing, synaptic function and morphometric properties of individual CLT and *MECP2* null neurons, we next sought to determine if neural circuit activity would be perturbed in RTT neurons. Isogenic WT and RTT *Ngn2* neurons were cocultured with mouse astrocytes on 12-well MEA plates with 64 channels in an 8x8 grid per well (Axion Biosystems) (Fig. 4A-C, top right). Every plate was derived from an independent differentiation and contained 3-6 wells of each isogenic genotype as technical replicates. Five minute recordings of extracellular spontaneous action potential activity were taken to acquire high frequency spikes twice per week from week 3 to 7. Bursting and network bursting properties emerged with maturation of the cultures over time at a comparable rate as induced neurons previously recorded by MEA (Deneault et al., 2019). Raster plots of the firing patterns show individual spikes (white tick marks), bursts and network bursts across multiple electrodes (pink tick marks) for the CLT, WIBR3 and PGPC14 isogenic pairs (Fig. 4A-C, left with inset). During the time course, the number of active electrodes and firing rate would be expected to increase as connections develop within the network. We used these metrics to assess the quality and distribution of the neurons in the wells on each plate, and only analyzed wells that passed a cut-off of at least 32 active electrodes (Fig. S4A). Additionally, at the final time point neurons were treated with the AMPAR antagonist CNXQ to show that spiking activity was abolished (Fig. S4B). These data support the conclusion that synaptic transmission was responsible for signalling throughout the network.

Based on the less affected electrophysiology and normal size of L124W neurons, we predicted that L124W neurons may not resemble network circuitry phenotypes of *MECP2* null neurons. To correct for different maturation dynamics that contribute to MEA plate-to-plate variability, we normalized the fold-change of RTT values to the respective WT isogenic values within a plate. We first examined 6 biological replicate plates of CLT isogenic neurons. The L124W *Ngn2* neurons did not demonstrate any changes in adjacent timepoints for weighted

bioRxiv preprint doi: https://doi.org/10.1101/2020.07.12.189621; this version posted July 12, 2020. The copyright holder for this preprint (which was not certified by peer review) is the author/funder. All rights reserved. No reuse allowed without permission.

mean firing rate which is normalized to the number of active electrodes per well, or network burst frequency or duration (Fig. 4D). To ensure that the MEA assay was capable of detecting circuitry defects in *MECP2* null neurons, we then examined 6 biological replicate plates of WIBR3 and 4 biological replicate plates of PGPC14 isogenic pairs. The weighted mean firing rate also did not have a consistent change in *MECP2* null neurons (Fig. 4E,F (i)). However, the *MECP2* null network bursts, which assess the connectivity of the neurons, showed a consistently deceased frequency beginning at the 4 week time-point. These decreased network burst frequencies were followed by longer network burst durations that transiently emerged at weeks 5-6 in WIBR3 and PGPC14 isogenic lines (Fig. 4E,F (ii,iii) & S4C,D). Overall, our findings show that single L124W neurons have electrophysiological deficits in patch clamp recordings and reduced dendritic complexity, but do not display altered circuitry detected by standard MEA metrics of recorded induced excitatory neurons. These L124W phenotypes are more nuanced than those recorded from isogenic pairs of *MECP2* null neurons, and our MEA results establish that the *MECP2* null mutations profoundly disturb the network burst frequency.

bioRxiv preprint doi: https://doi.org/10.1101/2020.07.12.189621; this version posted July 12, 2020. The copyright holder for this preprint (which was not certified by peer review) is the author/funder. All rights reserved. No reuse allowed without permission.

DISCUSSION

In this study, we defined a wide phenotypic spectrum of *MECP2* mutation-dependent changes in heterochromatin binding, neuron morphology, electrophysiological properties and network connectivity by modeling RTT neurons *in vitro*. We investigated the effects of a novel MECP2 L124W MBD variant in comparison with three *MECP2* nulls in isogenic induced excitatory neurons. Our findings uncover a subset of core functional and morphological phenotypes present in all lines and a broader set of additional impairments exhibited by null neurons. The subset of core phenotypes included higher input resistance, impaired Na^+ and K^+ evoked currents and less complex dendrites. *MECP2* null neurons consistently displayed depolarized resting membrane potential, reduced cell capacitance accompanied by decreased soma area and dendrite length, and had disruptions in neuronal network burst frequency and duration patterns. Thus, the *MECP2* null phenotypic profile encompassed known RTT-associated changes that validated our induced neuron model and revealed novel insights into the development of excitatory synaptic activity and network circuitry.

L124W molecular and functional shared phenotypes

The less severe RTT-associated phenotypic profile of L124W was supported by evidence of partially disrupted chromocenter binding in mouse cells and stable unchanged protein level in induced neurons. These indicated limited functionality of the produced L124W protein, which we would expect to have a less severe outcome than complete loss-of-function mutations. The novel L124W variant represents a subtype of MECP2 MBD mutation that retains partial function. This may serve as a precedent for the discovery of other partially functional missense variants that do not fully phenocopy the effects of *MECP2* null mutations in human neurons.

bioRxiv preprint doi: https://doi.org/10.1101/2020.07.12.189621; this version posted July 12, 2020. The copyright holder for this preprint (which was not certified by peer review) is the author/funder. All rights reserved. No reuse allowed without permission.

The limited alterations in morphology and electrophysiology, and lack of change in network circuitry by standard MEA metrics in L124W were unexpected given the previous studies on L124F and other disruptive MBD missense variants (Tillotson and Bird, 2019). One potential experimental artefact we excluded was XCI erosion in the CLT L124W iPSCs. Since expression of the X_i was not reactivated during continued passage, no WT MECP2 was produced to rescue L124W phenotypes. In a related protein level issue, MECP2 is known to be highly abundant and near histone-octamer levels in neurons (Skene et al., 2010). We observed that MECP2 level in induced *Ngn2* neurons was lower than NPC-derived neurons used as controls. This suggests that sub-optimal levels of MECP2 in induced neurons used for MEAs can reveal circuitry changes in *MECP2* null neurons, but standard MEA metrics may not be adequate to reveal potentially subtle changes in L124W neurons. We also recognize the possibility that L124W may have a more profound functional effect on other cell types. For example, RTT astrocytes have been shown to exert non-cell autonomous effects on WT and mutant neurons (Ballas et al., 2009; Williams et al., 2014). As inhibition was absent in our excitatory neuron model, co-culturing astrocytes with glutamatergic and GABAergic neurons in monolayers or organoids could explore the potential interplay of these signals in L124W network activity.

MECP2 null full phenotype and circuitry defects

We observed robust network bursting phenotypes exhibited by the *MECP2* null induced excitatory neurons in MEA. These results suggest that the circuitry phenotype may correlate most with cells that have firing impairments, reduced cell capacitance and smaller size, but not with the core subset of phenotypes shared with L124W neurons. The multi-unit spiking pattern changes revealed that network-wide events occurred less frequently and had extended burst trains in *MECP2* nulls compared to WT. This may be due to changes in the levels of neurotransmitter receptors on the cell membrane (Rodrigues et al., 2020) that contribute to

bioRxiv preprint doi: https://doi.org/10.1101/2020.07.12.189621; this version posted July 12, 2020. The copyright holder for this preprint (which was not certified by peer review) is the author/funder. All rights reserved. No reuse allowed without permission.

action potential firing properties, as seen in an human NPC-derived neuron model of RTT. This RTT circuitry phenotype shows similarity to the reduced rate and increased duration of network bursts observed in Kleefstra syndrome induced excitatory neural cultures cocultured with rodent astrocytes, where these changes were found to be mediated by upregulation of NMDAR subunit *GRIN1* expression (Frega et al., 2019). Highly perturbed RTT-associated oscillatory network activity phenotype in local field potential MEA recordings of isogenic WT and MECP2 knockout iPSC-derived cortical organoids showed complete absence of network events (Trujillo, Gao, Negraes et al, http://doi.org/10.1101/358622).

Surprisingly, the weighted mean firing rate based on spiking activity was not consistently changed in MEAs, and therefore is discordant with the decreased action potential numbers observed in single cell electrophysiology. This discrepancy could in part be due to plate-to-plate variability in MEA baseline firing that was observed in the neural cultures. It is also possible that recordings of patched single neurons may be over-represented in periods of reduced spiking found during the long inter-burst interval in RTT. In contrast, the longer time frame of MEA could compensate for this by capturing the elevated spike numbers found in several cycles of RTT network bursts.

The core subset of firing impairments included reduced K^+ channel evoked currents. We have recently shown that *MECP2* null neurons derived from NPCs not only have extensive changes in their transcriptome as is widely reported, but that the translatome is also dramatically altered (Li et al., 2013; Rodrigues et al., 2020). One consequence is that reduced translation of E3 ubiquitin ligases leads to increased protein levels of target K^+ channels and neuroreceptors in RTT neurons. We note that induced WT *Ngn2* neurons have a four-fold higher K^+ threshold than WT NPC derived neurons, but despite this elevated baseline *MECP2* nulls and L124W share the K^+ current defect. Taken together, the mechanisms underlying single

bioRxiv preprint doi: https://doi.org/10.1101/2020.07.12.189621; this version posted July 12, 2020. The copyright holder for this preprint (which was not certified by peer review) is the author/funder. All rights reserved. No reuse allowed without permission.

cell neurophysiology and disrupted network bursting activity in RTT neurons may be illuminated by further investigation into protein level changes in ion channel and neurotransmitter receptors.

Significance

In summary, we identified a wide range of RTT-associated phenotypes relating to form and function in isogenic human stem cell-derived excitatory neurons harbouring a novel L124W missense compared to *MECP2* null mutations. The striking network burst frequency changes revealed in *MECP2* null neurons provide a potentially screenable phenotype for testing candidate compounds to rescue the RTT-associated changes in this *in vitro* assay to moderate disease. However, full rescue might also require correction of the subset of core phenotypes found in L124W neurons that are detected by morphometry and single cell electrophysiology.

bioRxiv preprint doi: https://doi.org/10.1101/2020.07.12.189621; this version posted July 12, 2020. The copyright holder for this preprint (which was not certified by peer review) is the author/funder. All rights reserved. No reuse allowed without permission.

METHODS

Chromocenter and FRAP Assays

All imaging and image analysis were performed as previously described (Sheikh et al., 2017, 2016), with the following exception. FRAP Time-lapse imaging: A series of confocal time lapse images of frames (512 x 512 pixels) imaged at 488nm laser excitation with 0.05 transmission were used to record GFP-tagged protein post bleach recovery. FRAP assay was recorded with a minimum of nine pre-bleach frames, one frame after 1000 µs bleaching with 405 nm laser line at 100% transmission, and 90 post-bleach frames were recorded at equal time intervals.

iPSC Reprogramming

iPSCs were reprogrammed under approval of the Canadian Institutes of Health Research Stem Cell Oversight Committee and the Research Ethics Board of The Hospital for Sick Children (REB #1000050639) and the University of California San Diego (IRB #14123ZF).

iPSC lines were generated from fibroblasts. Fibroblasts were collected from a small incision in the skin after a skin biopsy and tissue was washed in PBS 1x with 4% penicillin/streptomycin (Gibco). Later, the tissue was broken into small pieces using needles and plated in culture media (DMEM/F12, 15% FBS, 1% MEM NEAA, 1% L-glutamine and 1% penicillin/streptomycin). After 1 month, fibroblasts migrated out from the tissue. After reaching high confluency, cells were expanded or frozen as stock (Beltrão-Braga et al., 2011; Fernandes et al., 2016). Fibroblasts were reprogrammed using Sendai virus (Invitrogen) in feeder-free conditions on Matrigel (Corning) with mTeSR1 (STEMCELL Technologies). After colonies started to grow, colonies were picked manually and expanded on feeder-free Matrigel-coated dishes and frozen with CryoStore (STEMCELL Technologies). Mycoplasma contamination was routinely checked.

iPSC/ESC Culturing

Human iPSC/ESCs were maintained on dishes coated with Matrigel in mTeSR1 or StemMACS iPS-Brew XF (Miltenyi Biotec) media with 1% penicillin/stretomycin. iPSCs were passaged weekly with ReLeSR (STEMCELL Technologies) with daily media changes except for the day following passaging. Accutase (Innovative Cell Technologies) and media with 10 µM Rho-associated kinase (ROCK) inhibitor (Y-27632, STEMCELL Technologies) was used for any single-cell dissociation. Routine mycoplasma testing was performed.

Karyotyping

iPSC karyotyping and standard G-banding chromosome analysis (400-banding resolution) was performed by The Centre for Applied Genomics (TCAG) at The Hospital for Sick Children.

Pluripotency Assays

iPSC colonies were fixed and stained with pluripotency markers OCT4, NANOG, SSEA4 and TRA-1-60. Following embryoid body formation and spontaneous 3-germ layer differentiation for 16 days, resulting cells were fixed and stained for α-SMA, AFP and β-III-tubulin. To assess gene expression profile of iPSCs, RNA was extracted from 1 confluent well of a 6-well plate using RNA PureLink RNA mini kit (Life Technologies) as per manufacturer's protocol. Samples were sent to TCAG at the Hospital for Sick Children for Bioanalyzer assessment and sequenced as paired end 2x125 bases on an Illumina HiSeq 2500 at a depth of 15M reads. Resulting FASTQ files were uploaded to www.pluritest.org for analysis (Müller et al., 2011). Files can be found with GEO accession GSE148435.

bioRxiv preprint doi: https://doi.org/10.1101/2020.07.12.189621; this version posted July 12, 2020. The copyright holder for this preprint (which was not certified by peer review) is the author/funder. All rights reserved. No reuse allowed without permission.

XCI Assays

Androgen receptor (AR) assay was performed as previously described (Cheung et al., 2011). In brief, 400 ng of genomic DNA from iPSCs/ESCs was digested by CpG methylation-sensitive restriction enzymes *HpaII* and *HhaI* for 6 hours. 2 µL of digestion was amplified using Platinum Taq DNA Polymerase High Fidelity (Invitrogen) with AR gene primers with a FAM label (Table 3). Male samples were used as a control to confirm complete digestion. Electrophoresis was performed by TCAG at The Hospital for Sick Children. Traces were analyzed using PeakScanner (Thermo Fisher Scientific). To identify which *MECP2* allele was expressed on the active X chromosome, RNA was isolated from iPSCs and reverse transcribed into cDNA using SuperScript III (Invitrogen). Primers flanking the variant region (Table 3) were used for amplification with Platinum Taq DNA Polymerase High Fidelity or Q5 High Fidelity DNA Polymerase (New England BioLabs), followed by cloning as per the TOPO TA Cloning Kit (Invitrogen) or Zero Blunt TOPO Cloning Kit (Invitrogen) in OneShot TOP10 (Thermo Fisher Scientific) or Max Efficiency DH5α (Invitrogen) competent *E. coli* strains. 5-10 bacterial colonies per iPSC cell line tested were picked and grown in LB Medium (MP Biomedicals) for DNA extraction with Quick Plasmid MiniPrep Kit (Invitrogen). Samples were Sanger sequenced at TCAG and aligned to WT MECP2 template using benchling.com.

CRISPR-Cas9 Gene Editing

The *MECP2* indel mutation was generated using a previously described gene editing strategy (Hildebrandt et al., 2019). Briefly, pSpCas9(BB)-2A-Puro (PX459) V2.0 (Addgene #62988) was cloned with an oligo designed to target *MECP2* exon 3 using benchling.com CRISPR prediction tool (Table 3). Indels were introduced by transfecting $8x10^5$ cells with 1.5 µg plasmid in 100 µl scale using the Neon Transfection System (ThermoFisher) with one pulse at 1500 millivolts for 30 milliseconds (~40-70% transfection efficiency). Transfected cells were plated in 2 wells of a 6-well plate with mTeSR1 media supplemented with CloneR (STEMCELL Technologies) to enhance cell survival. From D2-5, puromycin (0.5 ug/ml) was added to daily to mTeSR1 media changes and surviving single colonies were grown to D12-18 before transferring to 24-well plates. Isolated clones were passaged and gDNA was harvested with a Quick DNA miniprep kit (Zymo) and PCR products were sent for Sanger sequencing by TCAG at the Hospital for Sick Children.

Lentivirus Preparation and Transduction

FUW-TetO-Ngn2-P2A-EGFP-T2A-puromycin and FUW-rtTA plasmids for excitatory cortical neuron differentiations were kindly gifted by T. Sudhof (Zhang et al., 2013) and packaged as per a previously described protocol (Hotta et al., 2009). Lentiviruses were produced in HEK293T cells using a third generation packaging system (pMDG.2, pRSV-Rev and pMDLg/pRRE). Viral particles in the supernatant were collected 48 hours post-transfection, filtered and concentrated by 91,000 x g centrifugation for 2 hours at 4°C. For iPSC transductions, accutase (Innovative Cell Technologies) was used to obtain $5x10^5$ cells single-cells per well of a Matrigel-coated 6-well plate that were incubated with concentrated virus in mTeSR1 with 10 µM ROCK inhibitor and 8 µg/ml polybrene (Sigma) for 8 hours. Media was changed to mTeSR1 and transduced iPSCs were maintained and expanded to acquire frozen stocks.

Ngn2 Neuronal Differentiation

Excitatory cortical neurons were generated as previously described (Deneault et al., 2018; Hildebrandt et al., 2019). Briefly, on Day 0 iPSCs were made into single-cells by accutase and plated at $3x10^5$-$1x10^6$ cells per well on Matrigel-coated 6-well plates with StemMACS iPS-Brew XF media supplemented with 10 µM ROCK inhibitor. All media mentioned for Day 1-8 contained 1x penicillin/streptomycin (Gibco), 1 µg/mL laminin (Sigma), 2 µg/mL doxycycline

bioRxiv preprint doi: https://doi.org/10.1101/2020.07.12.189621; this version posted July 12, 2020. The copyright holder for this preprint (which was not certified by peer review) is the author/funder. All rights reserved. No reuse allowed without permission.

hyclate (Sigma), 10 ng/ml BDNF (Peprotech) and 10 ng/mL GDNF (Peprotech). On Day 1, media was changed to CM1 consisting of DMEM/F12 (Gibco), 1x N2 (Gibco) and 1x NEAA (Gibco), supplemented with 10 µM ROCK inhibitor. On Day 2, media was changed to CM1 supplemented with 2-5 µg/mL puromycin (Sigma). On Day 3, media was changed to CM2 consisting of Neurobasal (Gibco), 1x B27 (Gibco) and 1x Glutamax (Gibco), supplemented with 2-5 µg/mL puromycin. On Day 4-5, media was changed to CM2. On Day 6, media was changed to CM2 supplemented with 10 µM AraC (Sigma). On Day 8, doxycycline induction was withdrawn and neurons were re-seeded into new dishes in CM2 and co-cultured with P1 mouse astrocytes unless otherwise noted for downstream assays.

Protein Quantification

Protein was extracted from neurons (not grown with mouse astrocytes) washed in ice-cold PBS using radioimmune precipitation assay (RIPA) buffer (25 mM Tris-HCl, pH 7.6, 150 mM NaCl, 1% Nonidet P-40, 1% sodium deoxycholate and 0.1% SDS). Equivalent protein masses were loaded into capillaries for detection using the 12-230 kDa Separation Kit for the Wes (ProteinSimple). Multiplexed probing of MECP2 and β-actin by chemiluminescence was quantified using Compass for SW software (ProteinSimple).

Patch-Clamp Electrophysiology

Electrophysiological recordings were made as reported previously (Djuric et al., 2015; Farra et al., 2012). Briefly, whole-cell patch-clamp recordings were performed with an Axopatch 1-D amplifier (Molecular Devices, USA) operated with Clampex 9.2 software and a DigiData 1200 series interface (Molecular Devices, USA), and the currents were sampled at 10 kHz and filtered at 2 kHz. The recordings were analyzed off-line using Clampfit 9.2 software (Molecular Devices, USA). All electrophysiological experiments and data analysis were conducted with Ngn2 neuron samples blinded to the investigator. To examine intrinsic membrane properties, the recordings were performed in a 35-mm tissue culture dish filled with an extracellular solution containing (in mM): 140 NaCl, 5.4 KCl, 1 MgCl2, 15 HEPES, 2 CaCl2, 10 glucose, and the solution was adjusted to pH 7.35 with NaOH. Patch-clamp pipettes (5 to 8 MΩ) were pulled from capillary glass (1.5 mm diameter; World Precision Instruments, USA) using a P-87 pipette puller (Sutter Instrument Co., USA), and filled with an intracellular solution compose of (in mM): 144 K+-gluconate, 10 KCl, 2 Mg-ATP, 2 EGTA, 10 HEPES. The solution was adjusted to pH 7.2 with KOH. Voltage-gated ion currents, under the whole-cell voltage-clamp condition, were elicited at the holding membrane potential of -70 mV by stepping the membrane potential to a series of potentials from –80 mV to +60 mV for 400 ms. Action potentials, under current-clamp condition, were evoked from the membrane potential of around -75 mV by injecting a series of current steps. In current-clamp, we subtracted a liquid junction potential of 16 mV from the membrane potential values measured with K+-gluconate based intracellular solutions.
To investigate synaptic function, mEPSCs, in voltage-clamp, were recorded human Ngn2 neurons at the holding membrane potential of -60 mV. Recording micropipettes were filled with an intracellular solution as described above. The extracellular recording solutions consisted of (in mM): 140 NaCl, 1 MgCl2, 5.4 KCl, 1.3 CaCl2, 25 glucose, 15 HEPES, 0.003 glycine, 0.001 strychnine, 0.01 bicuculline, 0.0005 tetrodotoxin, and pH was adjusted to 7.35 with NaOH. mEPSCs were detected and analyzed off-line using Mini Analysis Program (Synaptosoft Inc, USA).

Neuron Labelling

Neurons were transfected with *pL-SIN-EF1α-eGFP* plasmid (Addgene 21320) using 1 µg of DNA and 2 µL of Lipofectamine 2000 (Thermo Fisher Scientific) per well of a 24-well plate. 48 hours post-transfection, neurons were fixed at 6 weeks and stained for MAP2 and GFP.

bioRxiv preprint doi: https://doi.org/10.1101/2020.07.12.189621; this version posted July 12, 2020. The copyright holder for this preprint (which was not certified by peer review) is the author/funder. All rights reserved. No reuse allowed without permission.

Immunocytochemistry (ICC)

iPSCs were fixed with 4% formaldehyde in PBS for 8 minutes at room temperature. Neurons grown on 12mm round glass coverslips (Bellco) or 24-well µ-Plates (Ibidi) were fixed with 4% formaldehyde in 0.4 M sucrose Krebs buffer for 8 minutes to preserve cytoskeletal integrity (Kwiatkowski et al., 2007). Fixed cells were permeabilized with 0.1% Triton X-100 for 8 minutes at room temperature and blocked for at least 1 hour at room temperature in ICC buffer (10% normal goat (Cedarlane) or donkey (Sigma) serum in PBS with 0.05% Tween 20). Primary antibodies were diluted in ICC buffer and incubated overnight at 4°C. Secondary antibodies were diluted in PBS with 0.05% Tween 20 and incubated for 1 hour at room temperature. Unless otherwise indicated, nuclei were counterstained with 1 µg/ml DAPI in PBS for 5 minutes at room temperature. If cells were on coverslips, they were rinsed in molecular grade water and mounted on slides in Prolong Gold antifade mounting media (Thermo Fisher). Details for primary antibodies used in this study can be found in Table 4.

Imaging

iPSC pluripotency and 3-germ layer assays were imaged with a Leica DM14000B epifluorescence microscope using a DFC7000T camera and LAS X software. Neurons for soma/dendrite tracing were imaged with an Olympus 1X81 spinning disk confocal microscope using a Hamamatsu C9100-13 EM-CDD camera and Volocity software (Perkin Elmer). Synapses were imaged with a Leica SP8 Lightning Confocal/Light Sheet point scanning confocal microscope and LAS X software.

Neuronal Morphometry

Blinded images were analyzed using Filament Tracer in Imaris (Bitplane) by two individuals. Soma were manually traced with semi-automated reconstruction of dendrites on sparsely GFP labeled neurons that were co-stained with MAP2 (3-5 replicate batches, total = 404 neurons).

MEA Plating and Recording

12-well CytoView MEA plates (Axion Biosystems) with 64 channels per well in 8x8 electrode grids were coated with filter sterilized 0.1% poly(ethylenimine) solution (Sigma) in borate buffer pH 8.4 for 1 hour at room temperature, washed 4 times with water and dried overnight. Day 8 differentiated Ngn2 neurons were re-seeded at a density of $1x10^5$ cells per 100 µL droplet in CM2 media consisting of BrainPhys (STEMCELL Technologies), 1x penicillin/streptomycin, 10 ng/ml BDNF and 10 ng/mL GDNF, supplemented with 400 µg/mL laminin and 10 µM ROCK inhibitor. Droplet of cells was applied directly on top of electrodes in each well, incubated for 1 hour at 37°C with hydration and then followed by slow addition of CM2 media supplemented with 10 µg/mL laminin. 24 hours later, $2x10^4$ P1 mouse astrocytes were seeded on top of the neurons in each well. CM2 media supplemented with 10 µg/mL laminin was changed consistently 24 hours prior to recording twice per week from 2 weeks onwards on the Maestro MEA platform (Axion Biosystems). Each plate was incubated for 5 minutes on a 37°C heated Maestro device, then recorded for 5 minutes of spontaneous neural activity using AxIS 2.0 software (Axion Biosystems) with a 0.2-3 kHz bandpass filter at 12.5 kHz sampling frequency. Spikes were detected at 6x the standard deviation of the noise on electrodes. Offline analysis used the Neural Metric Tool (Axion Biosystems), where an electrode was considered active if at least 5 spikes/min was detected. Poisson surprise burst and Envelope network burst algorithms with a threshold of at least 25% active electrode were applied. Further analyses and normalization of MEA metrics were completed in RStudio.

bioRxiv preprint doi: https://doi.org/10.1101/2020.07.12.189621; this version posted July 12, 2020. The copyright holder for this preprint (which was not certified by peer review) is the author/funder. All rights reserved. No reuse allowed without permission.

Statistical Analyses

Statistical tests for assays were performed in RStudio (v1.1.423) or GraphPad Prism. D'Agostino & Pearson test was used to determine normality for datasets. Comparisons within respective isogenic pairs were conducted by Student's t, one sample t or Mann-Whitney tests (* $p < 0.05$, ** $p < 0.01$, *** $p < 0.001$).

bioRxiv preprint doi: https://doi.org/10.1101/2020.07.12.189621; this version posted July 12, 2020. The copyright holder for this preprint (which was not certified by peer review) is the author/funder. All rights reserved. No reuse allowed without permission.

FIGURE CAPTIONS

Figure 1. Molecular impact of MECP2 L124W missense mutation and generation of iPSC lines.
A. MECP2 MBD 3D structure modeling L124W point mutation position relative to R106W.
B. Representative images of C2C12 mouse myoblast cells overexpressing WT-GFP and mutant MECP2-GFP fusion proteins stained with DAPI (blue) and GFP (green). Scale bar = 2 μm.
C. Quantification of chromocenter size and number and overlap by Pearson's correlation co-efficient (PCC). n = 15.
D. Representative images of FRAP time course for GFP and quantified fluorescence intensity of WT-GFP and L124W-GFP in C2C12 mouse cells. Scale bar = 2 μm.
E. Quantification of WT-GFP and L124W-GFP half-life and mobile fraction. n = 5.
F. Schematic showing position of *MECP2* mutations in the iPSC/ESC lines used in this study. Red line indicates location of deletion and red arrow indicates location of point or frameshift mutation.
G. Amplified peaks from PCR of polymorphic androgen receptor locus on the X active (X_a) or X inactive (X_i) for endonuclease digested and undigested gDNA samples from WT and *MECP2* mutant iPSC lines.
H. Sanger sequencing of cDNA for the CLT WT or c.371T>G (p.L124W) *MECP2* mutation from restricted expression of the active X chromosome in iPSC clones.
I. Digitized blot of isogenic *Ngn2* neurons and quantification of MECP2 protein level by capillary western in isogenic L124W *Ngn2* neurons normalized to β-actin. Mean with SEM, ns, $p > 0.05$. Indicated n/N = number of samples/number of replicates.
J. Wes capillary-based protein detection of MECP2 protein in 6 week old PGPC14 WT and null *Ngn2* neurons, compared to 4 week old d3-4 WT and null NPC-derived neurons.

Figure 2. Deficits in intrinsic membrane properties and excitatory synapse function in RTT neurons.
A. Patch-clamp recordings of individual 4-5 week old Ngn2 WT and *MECP2* null neurons with indicated n = # of neurons recorded, quantified for resting membrane potential,
B. Input resistance and
C. Cell capacitance.
D. Representative traces of evoked action potentials (APs) in 4-5 week old WT and *MECP2* null *Ngn2* neurons and quantification of AP numbers at a given injected current.
E. Quantification of Na^+ and K^+ currents in 4-5 week old WT and *MECP2* null *Ngn2* neurons at a given voltage.
F. Representative traces of AMPAR-mEPSCs in 6 week old WT and *MECP2* null *Ngn2* neurons and quantification of amplitude and frequency. Indicated n = # of neurons recorded. Mean with SEM, *** $p < 0.001$.
G. Patch-clamp recordings of individual 4-5 week old WT and L124W *Ngn2* neurons with indicated n = # of neurons recorded, quantified for resting membrane potential,
H. Input resistance and
I. Cell capacitance.
J. Representative traces of evoked action potentials (APs) in 4-5 week old WT and L124W *Ngn2* neurons and quantification of AP numbers at a given injected current.
K. Quantification of Na^+ and K^+ currents in 4-5 week old WT and L124W *Ngn2* neurons at a given voltage.
L. Representative traces of AMPAR-mEPSCs in 6 week old WT and L124W *Ngn2* neurons and quantification of amplitude and frequency. Indicated n = # of neurons recorded. Mean with SEM, *** $p < 0.001$.

bioRxiv preprint doi: https://doi.org/10.1101/2020.07.12.189621; this version posted July 12, 2020. The copyright holder for this preprint (which was not certified by peer review) is the author/funder. All rights reserved. No reuse allowed without permission.

Figure 3. RTT Ngn2-derived neurons have reduced size and complexity.
A. Representative images of 6 week old WT and *MECP2* mutant Ngn2 neurons co-cultured with mouse astrocytes. GFP sparse labelling (green), pan-neuronal marker MAP2 (magenta) and DAPI (blue). Scale bar = 100 μm.
B. Neurons quantified for soma area,
C. Total dendrite length and
D. Sholl complexity (10 μm increments). Mean with SEM, * $p < 0.05$. Indicated n/N = total number of neurons/number of replicate batches.

Figure 4. MECP2 null Ngn2 *neurons have altered network connectivity.*
A-C. Representative 120 second raster plots of action potential spikes (black tick marks), bursts (blue tick marks) and network bursting events (pink outline) from Ngn2 WT and *MECP2* mutant neurons co-cultured on mouse astrocytes at 5 weeks. Top right are representative images of 5-7 week old cultures on MEA electrodes. Bottom right are 5 second insets of example network burst events indicated by the outlined area on the raster plot.
D-F(i-iii). Log fold change of RTT relative to WT for all replicate plates (black bar = mean with SEM, dashed line shows where WT = 0) for weighted mean firing rate and network burst frequency and duration. 6 replicate plates of CLT, 6 replicate plates of WIBR3 and 4 replicate plates of PGPC14 with 3-6 wells per genotype per plate. Mean with SEM, * $p < 0.05$.

SUPPLEMENTAL FIGURE CAPTIONS

Figure S1. Generation of MECP2 L124W and PGPC14 MECP2 null iPSCs and Ngn2 excitatory cortical neurons.
A. G-band karyotyping of two CLT WT (C4 and C17) and two CLT L124W (C1 and C2) female iPSC lines (46XX).
B. Representative images of iPSC colonies from two CLT WT (C4 and C17) and two CLT L124W (C1 and C2) lines stained with pluripotency-associated nuclear markers OCT4 and NANOG (red) and surface markers SSEA4 and TRA-1-60 (green).
C. Representative images of spontaneous 3-germ layer embryoid body differentiations from two CLT WT (C4 and C17) and two CLT L124W (C1 and C2) iPSC lines stained with mesoderm marker SMA, ectoderm marker β-III-tubulin and endoderm marker AFP (green).
D. Pluritest clustering of two CLT WT (C4 and C17) and two CLT L124W (C1 and C2) iPSC colonies based on gene expression profile comparison to established iPSC lines.
E. Schematic of induced *Ngn2* neuronal differentiation protocol from iPSCs/ESCs.
F. G-band karyotyping of PGPC14 null iPSC line (46XX).
G. Representative images of iPSC colonies from PGPC14 null line stained with pluripotency-associated nuclear markers OCT4 and NANOG (green) and surface markers SSEA4 and TRA-1-60 (magenta). Scale bar = 100 μm.
H. Sanger sequencing of cDNA for the 1 bp insertion frameshift mutation (p.Val74CysfsTer16) from restricted expression of the active X chromosome CRISPR/Cas9 gene edited PGPC14 iPSCs.
I. Representative images of 6 week old PGPC14 WT and null *Ngn2* neurons co-cultured on mouse astrocytes stained with MECP2 (green) and MAP2 (magenta). Scale bar = 50 μm.
J. Western blot of MECP2 protein in 6 week old PGPC14 WT and null *Ngn2* neurons, compared to 4 week old d3-4 WT and null NPC-derived neurons.

bioRxiv preprint doi: https://doi.org/10.1101/2020.07.12.189621; this version posted July 12, 2020. The copyright holder for this preprint (which was not certified by peer review) is the author/funder. All rights reserved. No reuse allowed without permission.

Figure S2. Ngn2 neuron differentiation and action potential properties.
A. Action potential properties of 4-5 week old WT and *MECP2* null Ngn2 neurons.
B. Action potential properties of 4-5 week old WT and L124W *Ngn2* neurons combined and separated by clone. Mean with SEM, *** $p < 0.001$.

Figure S3. Branching alterations in RTT Ngn2 neurons.
A. Quantification of dendrite branching order, manual counting. Mean with SEM, * $p < 0.05$.

Figure S4. MEA properties in RTT Ngn2 neurons.
A. Number of active electrodes for isogenic WT and *MECP2* mutant *Ngn2* neurons over 3 to 7 weeks of individual replicate plates (number above indicates Plate ID). ,6 replicate plates of CLT, 6 replicate plates of WIBR3 and 4 replicate plates of PGPC14 with 3-6 wells per genotype per plate. Mean with SEM.
B. 10 week old WT and *MECP2* null *Ngn2* neurons treated with CNQX.
C-D. Network burst frequency and duration for isogenic WT and null *Ngn2* neurons over 3 to 7 weeks of individual replicate plates (number above indicates Plate ID). 6 replicate plates of WIBR3 and 4 replicate plates of PGPC14. Mean with SEM.

bioRxiv preprint doi: https://doi.org/10.1101/2020.07.12.189621; this version posted July 12, 2020. The copyright holder for this preprint (which was not certified by peer review) is the author/funder. All rights reserved. No reuse allowed without permission.

TABLES

Table 1. Summary of cell lines studied.

Individual	Cell Type	Genotype	# of Clones	*MECP2*$^{+/-}$ Mutation Description	Reference
CLT	iPSC	WT	2	Wild-type	This study
		L124W	2	Patient c.371T>G; L124W missense mutation in methyl binding domain	
d3-4	iPSC	WT	1	Wild-type	Cheung et al, 2011
		NULL	1	Patient indel disrupting exons 3 & 4	
WIBR3	ESC	WT	1	Wild-type	Li et al, 2013
		NULL	1	TALEN-edited deletion of exons 3 & 4	
PGPC14	iPSC	WT	1	Wild-type	Hildebrandt et al, 2019
		NULL	1	CRISPR/Cas9-edited 1 bp insertion (frameshift, premature stop codon)	This study

Table 2. Summary of Ngn2 neuron phenotypes.
↑ = increased in RTT compared to WT; ↓ = decreased in RTT compared to WT

	Cell Line/*MECP2* Mutation			
	d3-4 Null	**WIBR3 Null**	**PGPC14 Null**	**CLT L124W**
DNA Binding				
Chromocenters				Disrupted
FRAP				↑ Recovery
Intrinsic Membrane Properties				
Resting membrane potential	↑	↑		No change
Input resistance	↑	↑		↑
Cell capacitance	↓	↓		No change
Evoked AP number	↓	↓		↓ Trend
Na^+/K^+ currents	↓	↓		↓
mEPSC amplitude	↓	↓		↓ Trend
mEPSC frequency	↓	↓		↓ Trend
AP amplitude	No change	No change		No change
AP threshold	No change	↑		No change
AP rise time	↑	No change		No change
AP $D_{1/2}$	No change	No change		No change
AP decay	No change	No change		No change
Morphology				
Soma area	↓	↓	↓	No change
Dendrite length	↓	↓	↓	No change
Complexity	↓	↓	↓	↓
Network Circuitry				
Weighted mean firing rate		No change	No change	No change
Network burst frequency		↓	↓	No change
Network burst duration		↑	↑	No change

bioRxiv preprint doi: https://doi.org/10.1101/2020.07.12.189621; this version posted July 12, 2020. The copyright holder for this preprint (which was not certified by peer review) is the author/funder. All rights reserved. No reuse allowed without permission.

Table 3. Oligonucleotides used in this study.

Application	**Target**	**FWD (5'-3')**	**REV (5'-3-)**	**Source**
XCI	*AR*	CGTGCGCGAAGTGATCCAGA	GTTTCTTTGCTGCTGCCTGGGGCTAGT	PMID: 21372149
cDNA sequencing	*MECP2*	GCTCCATAAAAATACAGACTCAC	TTTGGGCTTCTTAGGTGGTTT	This study
CRISPR sgRNA	*MECP2*	AGAAGCTTCCGGCACAGCCG		This study

Table 4. Primary antibodies used in this study.

Antibody	**Species**	**Dilution**		**Source**	**Cat #**
		ICC	**Wes**		
Anti-α-SMA	Mouse	1:200		Invitrogen	18-0106
Anti-β-actin	Mouse		1:500	Sigma	A5441
Anti-β-III tubulin	Mouse	1:200		Chemicon	MAB1637
Anti-AFP	Mouse	1:200		R&D	MAB1368
Anti-GFP	Chicken	1:1000		Thermo Fisher	A10262
Anti-HOMER1	Guinea pig	1:500		Synaptic Systems	160004
Anti-MAP2	Mouse	1:1000		Sigma	M1406
Anti-MAP2	Guinea pig	1:1000		Synaptic Systems	188004
Anti-MECP2	Rabbit	1:1000	1:50	Cell Signalling	3456 (D4F3) XP
Anti-Nanog	Rabbit	1:200		Cell Signalling	4903P
Anti-OCT4	Rabbit	1:200		Abcam	ab19857
Anti-SSEA4	Mouse	1:100		Invitrogen	41-4000
Anti-SYN1	Rabbit	1:200		Millipore	AB1543P
Anti-TRA-1-60	Mouse	1:100		Invitrogen	41-1000

bioRxiv preprint doi: https://doi.org/10.1101/2020.07.12.189621; this version posted July 12, 2020. The copyright holder for this preprint (which was not certified by peer review) is the author/funder. All rights reserved. No reuse allowed without permission.

REFERENCES

Agarwal, N., Becker, A., Jost, K., Haase, S., Thakur, B.K., Brero, A., Hardt, T., Kudo, S., Leonhardt, H., Cardoso, M., 2011. MeCP2 Rett mutations affect large scale chromatin organization. Hum. Mol. Genet. 20, 4187–95. https://doi.org/10.1093/hmg/ddr346

Amir, R.E., Van den Veyver, I.B., Wan, M., Tran, C.Q., Francke, U., Zoghbi, H.Y., 1999. Rett syndrome is caused by mutations in X-linked MECP2, encoding methyl-CpG-binding protein 2. Nat Genet 23, 185–188. https://doi.org/10.1038/13810

Ananiev, G., Williams, E.C., Li, H., Chang, Q., 2011. Isogenic Pairs of Wild Type and Mutant Induced Pluripotent Stem Cell (iPSC) Lines from Rett Syndrome Patients as In Vitro Disease Model. PLoS ONE 6, e25255. https://doi.org/10.1371/journal.pone.0025255

Archer, H., Evans, J., Leonard, H., Colvin, L., Ravine, D., Christodoulou, J., Williamson, S., Charman, T., Bailey, M.E.S., Sampson, J., de Klerk, N., Clarke, A., 2006. Correlation between clinical severity in patients with Rett syndrome with a p.R168X or p.T158M MECP2 mutation, and the direction and degree of skewing of X-chromosome inactivation. Journal of Medical Genetics 44, 148–152. https://doi.org/10.1136/jmg.2006.045260

Ballas, N., Lioy, D.T., Grunseich, C., Mandel, G., 2009. Non-cell autonomous influence of MeCP2-deficient glia on neuronal dendritic morphology. Nat. Neurosci. 12, 311–7. https://doi.org/10.1038/nn.2275

Beltrão-Braga, P.C.B., Pignatari, G.C., Maiorka, P.C., Oliveira, N.A.J., Lizier, N.F., Wenceslau, C.V., Miglino, M.A., Muotri, A.R., Kerkis, I., 2011. Feeder-Free Derivation of Induced Pluripotent Stem Cells from Human Immature Dental Pulp Stem Cells. Cell Transplant 20, 1707–1719. https://doi.org/10.3727/096368911X566235

Buchovecky, C.M., Turley, S.D., Brown, H.M., Kyle, S.M., G, M., Jeffrey, Liu, B., Pieper, A.A., Huang, W., Katz, D.M., Russell, D.W., Shendure, J., Justice, M.J., 2013. A suppressor screen in Mecp2 mutant mice implicates cholesterol metabolism in Rett syndrome. Nat. Genet. 45, 1013–20. https://doi.org/10.1038/ng.2714

Chahrour, M., Jung, S.Y., Shaw, C., Zhou, X., Wong, S.T., Qin, J., Zoghbi, H.Y., 2008. MeCP2, a key contributor to neurological disease, activates and represses transcription. Science 320, 1224–9. https://doi.org/10.1126/science.1153252

Chahrour, M., Zoghbi, H.Y., 2007. The Story of Rett Syndrome: From Clinic to Neurobiology. Neuron 56, 422–437. https://doi.org/10.1016/j.neuron.2007.10.001

Cheung, A.Y., Horvath, L.M., Grafodatskaya, D., Pasceri, P., Weksberg, R., Hotta, A., Carrel, L., Ellis, J., 2011. Isolation of MECP2-null Rett Syndrome patient hiPS cells and isogenic controls through X-chromosome inactivation. Hum. Mol. Genet. 20, 2103–15. https://doi.org/10.1093/hmg/ddr093

Cohen, S., Gabel, H.W., Hemberg, M., Hutchinson, A.N., Sadacca, L., Ebert, D.H., Harmin, D.A., Greenberg, R.S., Verdine, V.K., Zhou, Z., Wetsel, W.C., West, A.E., Greenberg, M.E., 2011. Genome-wide activity-dependent MeCP2 phosphorylation regulates nervous system development and function. Neuron 72, 72–85. https://doi.org/10.1016/j.neuron.2011.08.022

Dani, V.S., Chang, Q., Maffei, A., Turrigiano, G.G., Jaenisch, R., Nelson, S.B., 2005. Reduced cortical activity due to a shift in the balance between excitation and inhibition in a mouse model of Rett Syndrome. Proceedings of the National Academy of Sciences 102, 12560–12565. https://doi.org/10.1073/pnas.0506071102

Deneault, E., Faheem, M., White, S.H., Rodrigues, D.C., Sun, S., Wei, W., Piekna, A., Thompson, T., Howe, J.L., Chalil, L., Kwan, V., Walker, S., Pasceri, P., Roth, F.P., Yuen, R.K., Singh, K.K., Ellis, J., Scherer, S.W., 2019. CNTN5- /+ or EHMT2- /+ human iPSC-derived neurons from individuals with autism develop hyperactive neuronal networks. Elife 8, e40092. https://doi.org/10.7554/eLife.40092

bioRxiv preprint doi: https://doi.org/10.1101/2020.07.12.189621; this version posted July 12, 2020. The copyright holder for this preprint (which was not certified by peer review) is the author/funder. All rights reserved. No reuse allowed without permission.

Deneault, E., White, S.H., Rodrigues, D.C., Ross, P., Faheem, M., Zaslavsky, K., Wang, Z., Alexandrova, R., Pellecchia, G., Wei, W., Piekna, A., Kaur, G., Howe, J.L., Kwan, V., Thiruvahindrapuram, B., Walker, S., Lionel, A.C., Pasceri, P., Merico, D., Yuen, R.K.C.K., Singh, K.K., Ellis, J., Scherer, S.W., 2018. Complete Disruption of Autism-Susceptibility Genes by Gene Editing Predominantly Reduces Functional Connectivity of Isogenic Human Neurons. Stem Cell Reports 11, 1211–1225. https://doi.org/10.1016/j.stemcr.2018.10.003

Djuric, U., Cheung, A.Y.L., Zhang, W., Mok, R.S., Lai, W., Piekna, A., Hendry, J.A., Ross, P.J., Pasceri, P., Kim, D.-S., Salter, M.W., Ellis, J., 2015. MECP2e1 isoform mutation affects the form and function of neurons derived from Rett syndrome patient iPS cells. Neurobiology of Disease 76, 37–45. https://doi.org/10.1016/j.nbd.2015.01.001

Farra, N., Zhang, W.-B.B., Pasceri, P., Eubanks, J., Salter, M., Ellis, J., 2012. Rett syndrome induced pluripotent stem cell-derived neurons reveal novel neurophysiological alterations. Mol. Psychiatry 17, 1261–71. https://doi.org/10.1038/mp.2011.180

Fernandes, I.R., Russo, F.B., Pignatari, G.C., Evangelinellis, M.M., Tavolari, S., Muotri, A.R., Beltrão-Braga, P.C.B., 2016. Fibroblast sources: Where can we get them? Cytotechnology 68, 223–228. https://doi.org/10.1007/s10616-014-9771-7

Frega, M., Linda, K., Keller, J.M., Gümüş-Akay, G., Mossink, B., van Rhijn, J.-R., Negwer, M., Klein Gunnewiek, T., Foreman, K., Kompier, N., Schoenmaker, C., van den Akker, W., van der Werf, I., Oudakker, A., Zhou, H., Kleefstra, T., Schubert, D., van Bokhoven, H., Nadif Kasri, N., 2019. Neuronal network dysfunction in a model for Kleefstra syndrome mediated by enhanced NMDAR signaling. Nat Commun 10, 4928. https://doi.org/10.1038/s41467-019-12947-3

Georgel, P.T., Horowitz-Scherer, R.A., Adkins, N., Woodcock, C.L., Wade, P.A., Hansen, J.C., 2003. Chromatin Compaction by Human MeCP2: Assembly of novel secondary chromatin structures in the absence of DNA methylation. J. Biol. Chem. 278, 32181–32188. https://doi.org/10.1074/jbc.M305308200

Hildebrandt, M.R., Reuter, M.S., Wei, W., Tayebi, N., Liu, J., Sharmin, S., Mulder, J., Lesperance, L.S., Brauer, P.M., Mok, R.S.F., Kinnear, C., Piekna, A., Romm, A., Howe, J., Pasceri, P., Meng, G., Rozycki, M., Rodrigues, D.C., Martinez, E.C., Szego, M.J., Zúñiga-Pflücker, J.C., Anderson, M.K., Prescott, S.A., Rosenblum, N.D., Kamath, B.M., Mital, S., Scherer, S.W., Ellis, J., 2019. Precision Health Resource of Control iPSC Lines for Versatile Multilineage Differentiation. Stem Cell Reports 13, 1126–1141. https://doi.org/10.1016/j.stemcr.2019.11.003

Ho, K.L., McNae, I.W., Schmiedeberg, L., Klose, R.J., Bird, A.P., Walkinshaw, M.D., 2008. MeCP2 Binding to DNA Depends upon Hydration at Methyl-CpG. Molecular Cell 29, 525–531. https://doi.org/10.1016/j.molcel.2007.12.028

Hotta, A., Cheung, A.Y.L., Farra, N., Garcha, K., Chang, W.Y., Pasceri, P., Stanford, W.L., Ellis, J., 2009. EOS lentiviral vector selection system for human induced pluripotent stem cells. Nat Protoc 4, 1828–1844. https://doi.org/10.1038/nprot.2009.201

Kim, K.-Y.Y., Hysolli, E., Park, I.-H.H., 2011. Neuronal maturation defect in induced pluripotent stem cells from patients with Rett syndrome. Proc. Natl. Acad. Sci. U.S.A. 108, 14169–74. https://doi.org/10.1073/pnas.1018979108

Knudsen, G.P.S., Neilson, T.C.S., Pedersen, J., Kerr, A., Schwartz, M., Hulten, M., Bailey, M.E.S., Ørstavik, K.H., 2006. Increased skewing of X chromosome inactivation in Rett syndrome patients and their mothers. Eur J Hum Genet 14, 1189–1194. https://doi.org/10.1038/sj.ejhg.5201682

Krishnaraj, R., Ho, G., Christodoulou, J., 2017. RettBASE: Rett syndrome database update. Hum. Mutat. 38, 922–931. https://doi.org/10.1002/humu.23263

bioRxiv preprint doi: https://doi.org/10.1101/2020.07.12.189621; this version posted July 12, 2020. The copyright holder for this preprint (which was not certified by peer review) is the author/funder. All rights reserved. No reuse allowed without permission.

Kudo, S., 2003. Heterogeneity in residual function of MeCP2 carrying missense mutations in the methyl CpG binding domain. Journal of Medical Genetics 40, 487–493. https://doi.org/10.1136/jmg.40.7.487

Kwiatkowski, A.V., Rubinson, D.A., Dent, E.W., Edward van Veen, J., Leslie, J.D., Zhang, J., Mebane, L.M., Philippar, U., Pinheiro, E.M., Burds, A.A., Bronson, R.T., Mori, S., Fässler, R., Gertler, F.B., 2007. Ena/VASP Is Required for Neuritogenesis in the Developing Cortex. Neuron 56, 441–455. https://doi.org/10.1016/j.neuron.2007.09.008

Li, Y., Wang, H., Muffat, J., Cheng, A.W., Orlando, D.A., Lovén, J., Kwok, S., Feldman, D.A., Bateup, H.S., Gao, Q., Hockemeyer, D., Mitalipova, M., Lewis, C.A., Vander Heiden, M.G., Sur, M., Young, R.A., Jaenisch, R., 2013. Global Transcriptional and Translational Repression in Human Embryonic Stem Cell-Derived Rett Syndrome Neurons. Cell Stem Cell 13, 446–458. https://doi.org/10.1016/j.stem.2013.09.001

Marchetto, M.C., Carromeu, C., Acab, A., Yu, D., Yeo, G.W., Mu, Y., Chen, G., Gage, F.H., Muotri, A.R., 2010. A model for neural development and treatment of Rett syndrome using human induced pluripotent stem cells. Cell 143, 527–39. https://doi.org/10.1016/j.cell.2010.10.016

Mekhoubad, S., Bock, C., de Boer, A.S., Kiskinis, E., Meissner, A., Eggan, K., 2012. Erosion of Dosage Compensation Impacts Human iPSC Disease Modeling. Cell Stem Cell 10, 595–609. https://doi.org/10.1016/j.stem.2012.02.014

Mellios, N., Feldman, D.A., Sheridan, S.D., Ip, J.P.K., Kwok, S., Amoah, S.K., Rosen, B., Rodriguez, B.A., Crawford, B., Swaminathan, R., Chou, S., Li, Y., Ziats, M., Ernst, C., Jaenisch, R., Haggarty, S.J., Sur, M., 2018. MeCP2-regulated miRNAs control early human neurogenesis through differential effects on ERK and AKT signaling. Mol Psychiatry 23, 1051–1065. https://doi.org/10.1038/mp.2017.86

Müller, F.-J., Schuldt, B.M., Williams, R., Mason, D., Altun, G., Papapetrou, E.P., Danner, S., Goldmann, J.E., Herbst, A., Schmidt, N.O., Aldenhoff, J.B., Laurent, L.C., Loring, J.F., 2011. A bioinformatic assay for pluripotency in human cells. Nat Methods 8, 315–317. https://doi.org/10.1038/nmeth.1580

Nageshappa, S., Carromeu, C., Trujillo, C., Mesci, P., I, E.-C., Pasciuto, E., Vanderhaeghen, P., Verfaillie, C., Raitano, S., Kumar, A., Carvalho, C., Bagni, C., Ramocki, M., Araujo, B., Torres, L., Lupski, J., Van Esch, H., Muotri, A., 2016. Altered neuronal network and rescue in a human MECP2 duplication model. Mol. Psychiatry 21, 178–88. https://doi.org/10.1038/mp.2015.128

Nan, X., Campoy, F.J., Bird, A., 1997. MeCP2 Is a Transcriptional Repressor with Abundant Binding Sites in Genomic Chromatin. Cell 88, 471–481. https://doi.org/10.1016/S0092-8674(00)81887-5

Nelson, E.D., Kavalali, E.T., Monteggia, L.M., 2006. MeCP2-Dependent Transcriptional Repression Regulates Excitatory Neurotransmission. Current Biology 16, 710–716. https://doi.org/10.1016/j.cub.2006.02.062

Rodrigues, D.C., Mufteev, M., Weatheritt, R.J., Djuric, U., Ha, K.C.H., Ross, P.J., Wei, W., Piekna, A., Sartori, M.A., Byres, L., Mok, R.S.F., Zaslavsky, K., Pasceri, P., Diamandis, P., Morris, Q., Blencowe, B.J., Ellis, J., 2020. Shifts in Ribosome Engagement Impact Key Gene Sets in Neurodevelopment and Ubiquitination in Rett Syndrome. Cell Reports 30, 4179-4196.e11. https://doi.org/10.1016/j.celrep.2020.02.107

Scala, E., Longo, I., Ottimo, F., Speciale, C., Sampieri, K., Katzaki, E., Artuso, R., Mencarelli, M.A., D'Ambrogio, T., Vonella, G., Zappella, M., Hayek, G., Battaglia, A., Mari, F., Renieri, A., Ariani, F., 2007. MECP2 deletions and genotype–phenotype correlation in Rett syndrome. American Journal of Medical Genetics Part A 143A, 2775–2784. https://doi.org/10.1002/ajmg.a.32002

bioRxiv preprint doi: https://doi.org/10.1101/2020.07.12.189621; this version posted July 12, 2020. The copyright holder for this preprint (which was not certified by peer review) is the author/funder. All rights reserved. No reuse allowed without permission.

Shahbazian, M.D., 2002. Insight into Rett syndrome: MeCP2 levels display tissue- and cell-specific differences and correlate with neuronal maturation. Human Molecular Genetics 11, 115–124. https://doi.org/10.1093/hmg/11.2.115

Sheikh, T.I., Ausió, J., Faghfoury, H., Silver, J., Lane, J.B., Eubanks, J.H., Patrick, M., Percy, A.K., Vincent, J.B., 2016. From Function to Phenotype: Impaired DNA Binding and Clustering Correlates with Clinical Severity in Males with Missense Mutations in MECP2. Sci Rep 6, 38590. https://doi.org/10.1038/srep38590

Sheikh, T.I., de Paz, A.M., Akhtar, S., Ausió, J., Vincent, J.B., 2017. MeCP2_E1 N-terminal modifications affect its degradation rate and are disrupted by the Ala2Val Rett mutation. Hum. Mol. Genet. 26, 4132–4141. https://doi.org/10.1093/hmg/ddx300

Skene, P.J., Illingworth, R.S., Webb, S., Kerr, A.R.W., James, K.D., Turner, D.J., Andrews, R., Bird, A.P., 2010. Neuronal MeCP2 Is Expressed at Near Histone-Octamer Levels and Globally Alters the Chromatin State. Molecular Cell 37, 457–468. https://doi.org/10.1016/j.molcel.2010.01.030

Tang, X., Drotar, J., Li, K., Clairmont, C.D., Brumm, A.S., Sullins, A.J., Wu, H., Liu, X.S., Wang, J., Gray, N.S., Sur, M., Jaenisch, R., 2019. Pharmacological enhancement of KCC2 gene expression exerts therapeutic effects on human Rett syndrome neurons and Mecp2 mutant mice. Sci. Transl. Med. 11, eaau0164. https://doi.org/10.1126/scitranslmed.aau0164

Tillotson, R., Bird, A., 2019. The Molecular Basis of MeCP2 Function in the Brain. Journal of Molecular Biology S0022283619305959. https://doi.org/10.1016/j.jmb.2019.10.004

Williams, E.C., Zhong, X., Mohamed, A., Li, R., Liu, Y., Dong, Q., Ananiev, G.E., Mok, J.C.C., Lin, B.R., Lu, J., Chiao, C., Cherney, R., Li, H., Zhang, S.-C.C., Chang, Q., 2014. Mutant astrocytes differentiated from Rett syndrome patients-specific iPSCs have adverse effects on wild-type neurons. Hum. Mol. Genet. 23, 2968–80. https://doi.org/10.1093/hmg/ddu008

Zhang, Y., Pak, C., Han, Y., Ahlenius, H., Zhang, Z., Chanda, S., Marro, S., Patzke, C., Acuna, C., Covy, J., Xu, W., Yang, N., Danko, T., Chen, L., Wernig, M., Südhof, T.C., 2013. Rapid Single-Step Induction of Functional Neurons from Human Pluripotent Stem Cells. Neuron 78, 785–798. https://doi.org/10.1016/j.neuron.2013.05.029

Figure 1

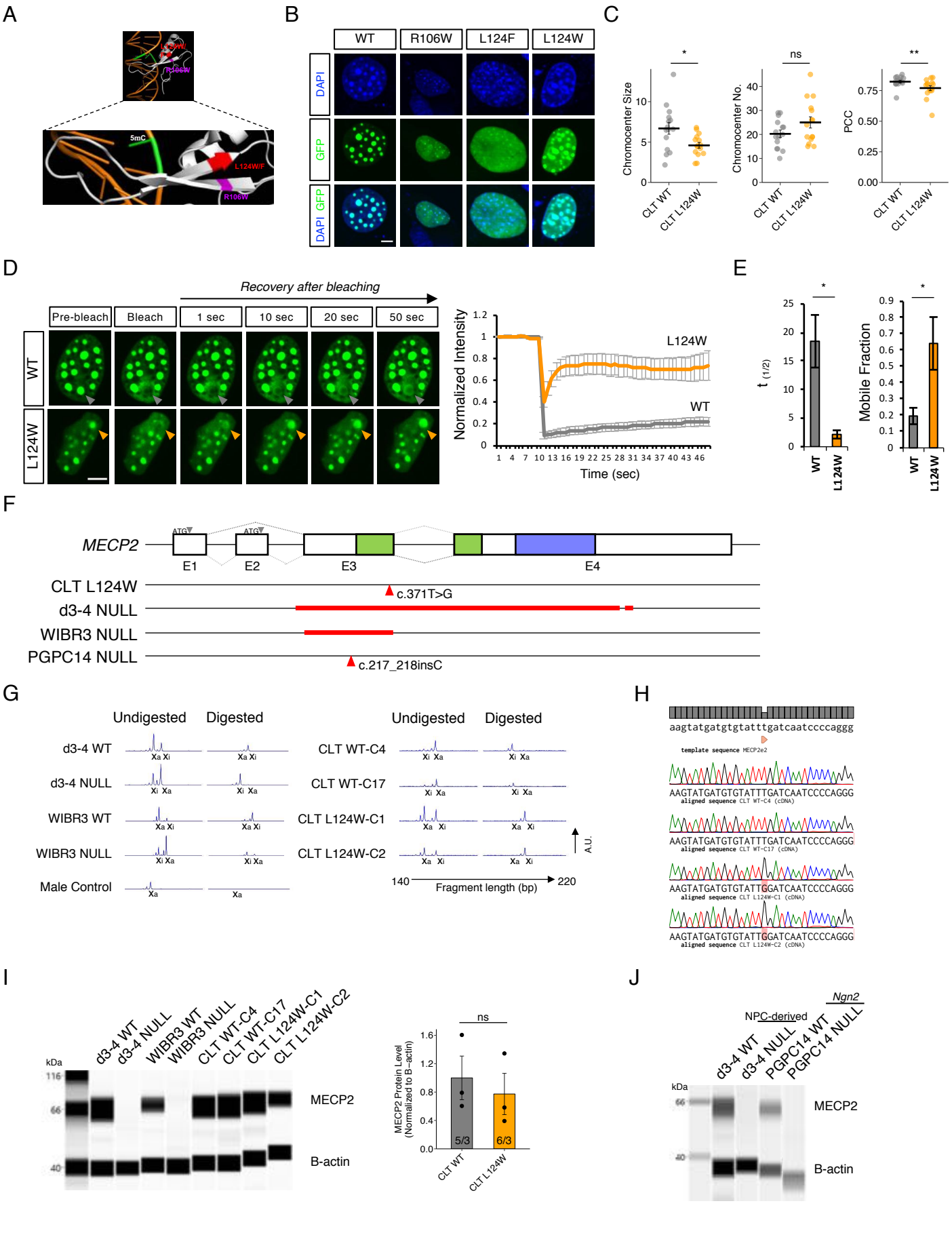
A
5mC
L124W/F
R106W
B
WT
R106W
L124F
L124W
DAPI
GFP
DAPI GFP
C
Chromocenter Size
Chromocenter No.
PCC
ns
CLT WT
CLT L124W
D
Recovery after bleaching
Pre-bleach
Bleach
1 sec
10 sec
20 sec
50 sec
WT
L124W
Normalized Intensity
Time (sec)
E
t (1/2)
Mobile Fraction
F
MECP2
ATG
E1
E2
E3
E4
CLT L124W
c.371T>G
d3-4 NULL
WIBR3 NULL
PGPC14 NULL
c.217_218insC
G
Undigested
Digested
d3-4 WT
d3-4 NULL
WIBR3 WT
WIBR3 NULL
Male Control
CLT WT-C4
CLT WT-C17
CLT L124W-C1
CLT L124W-C2
A.U.
140
Fragment length (bp)
220
H
aagtatgatgtgtatttgatcaatccccaggg
template sequence MECP2e2
AAGTATGATGTGTATTTGATCAATCCCCAGGG
aligned sequence CLT WT-C4 (cDNA)
aligned sequence CLT WT-C17 (cDNA)
aligned sequence CLT L124W-C1 (cDNA)
aligned sequence CLT L124W-C2 (cDNA)
I
kDa
116
66
40
MECP2
B-actin
MECP2 Protein Level (Normalized to B-actin)
5/3
6/3
J
Ngn2
NPC-derived
PGPC14 WT
PGPC14 NULL

Figure 2

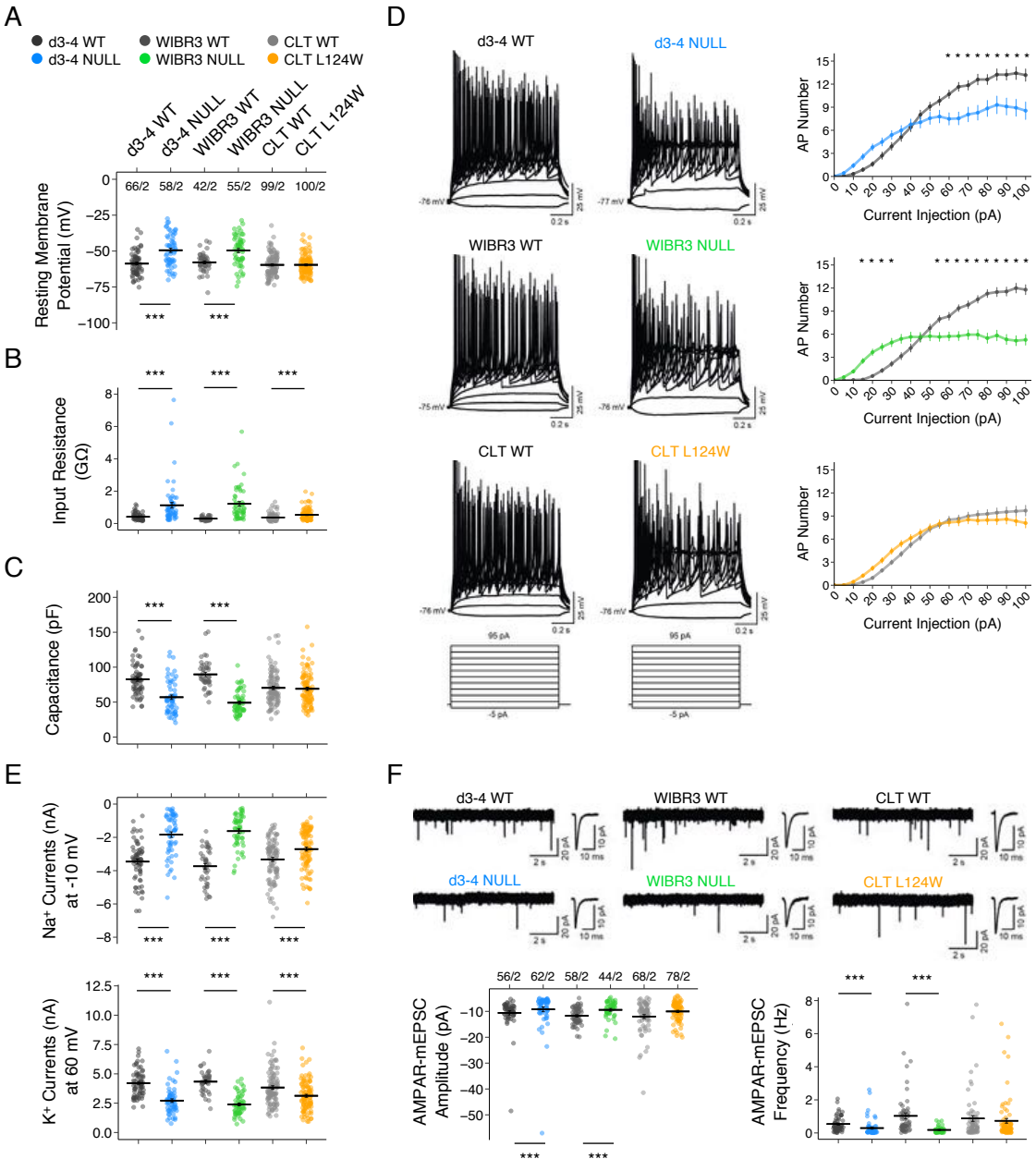
A
d3-4 WT
d3-4 NULL
WIBR3 WT
WIBR3 NULL
CLT WT
CLT L124W
Resting Membrane Potential (mV)
66/2 58/2 42/2 55/2 99/2 100/2
B
Input Resistance (GΩ)
C
Capacitance (pF)
D
AP Number
Current Injection (pA)
E
Na+ Currents (nA) at -10 mV
K+ Currents (nA) at 60 mV
F
AMPAR-mEPSC Amplitude (pA)
56/2 62/2 58/2 44/2 68/2 78/2
AMPAR-mEPSC Frequency (Hz)

Figure 3

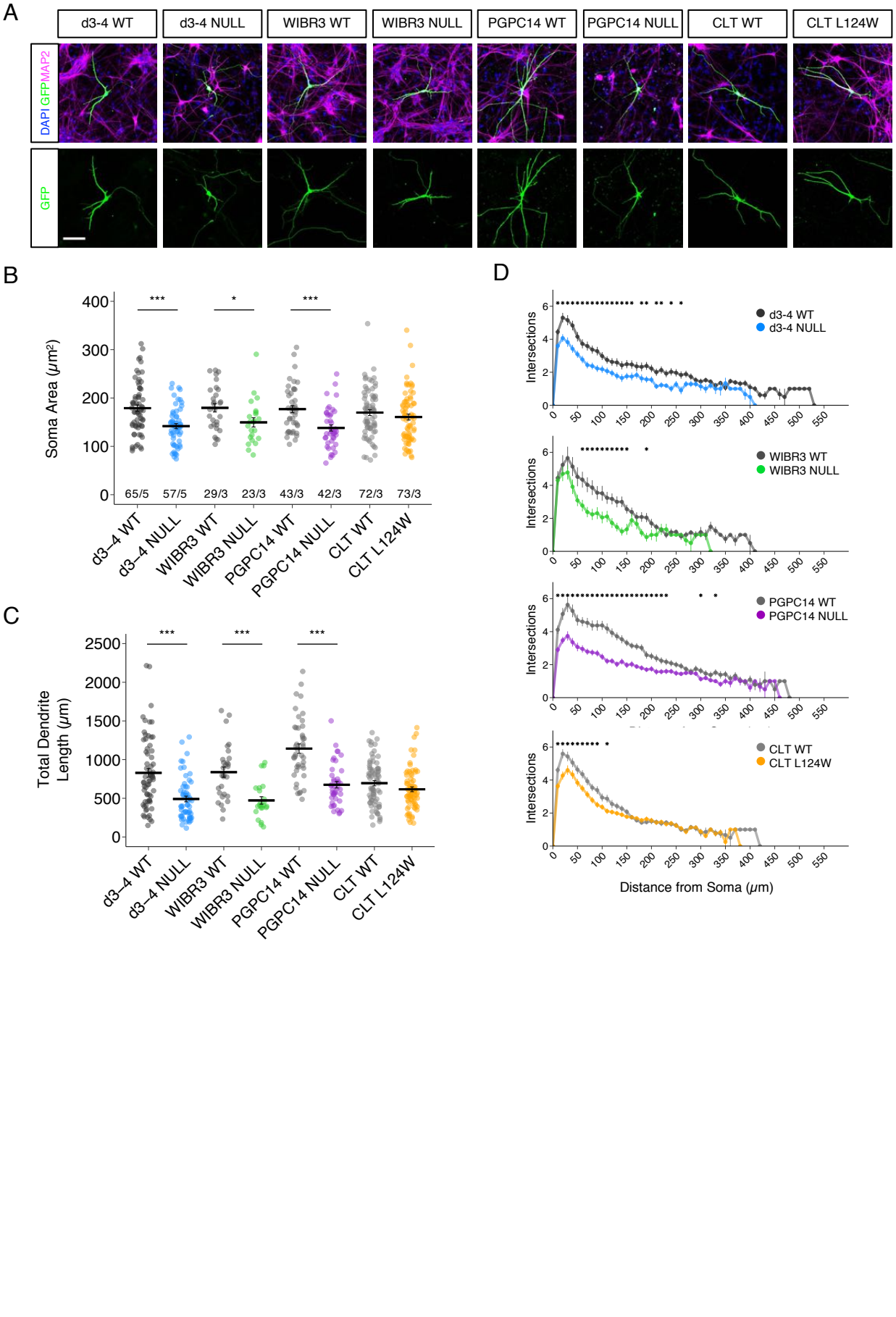
A
d3-4 WT
d3-4 NULL
WIBR3 WT
WIBR3 NULL
PGPC14 WT
PGPC14 NULL
CLT WT
CLT L124W
DAPI GFP MAP2
GFP
B
Soma Area (μm²)
65/5
57/5
29/3
23/3
43/3
42/3
72/3
73/3
C
Total Dendrite Length (μm)
D
Intersections
d3-4 WT
d3-4 NULL
WIBR3 WT
WIBR3 NULL
PGPC14 WT
PGPC14 NULL
CLT WT
CLT L124W
Distance from Soma (μm)

Figure 4

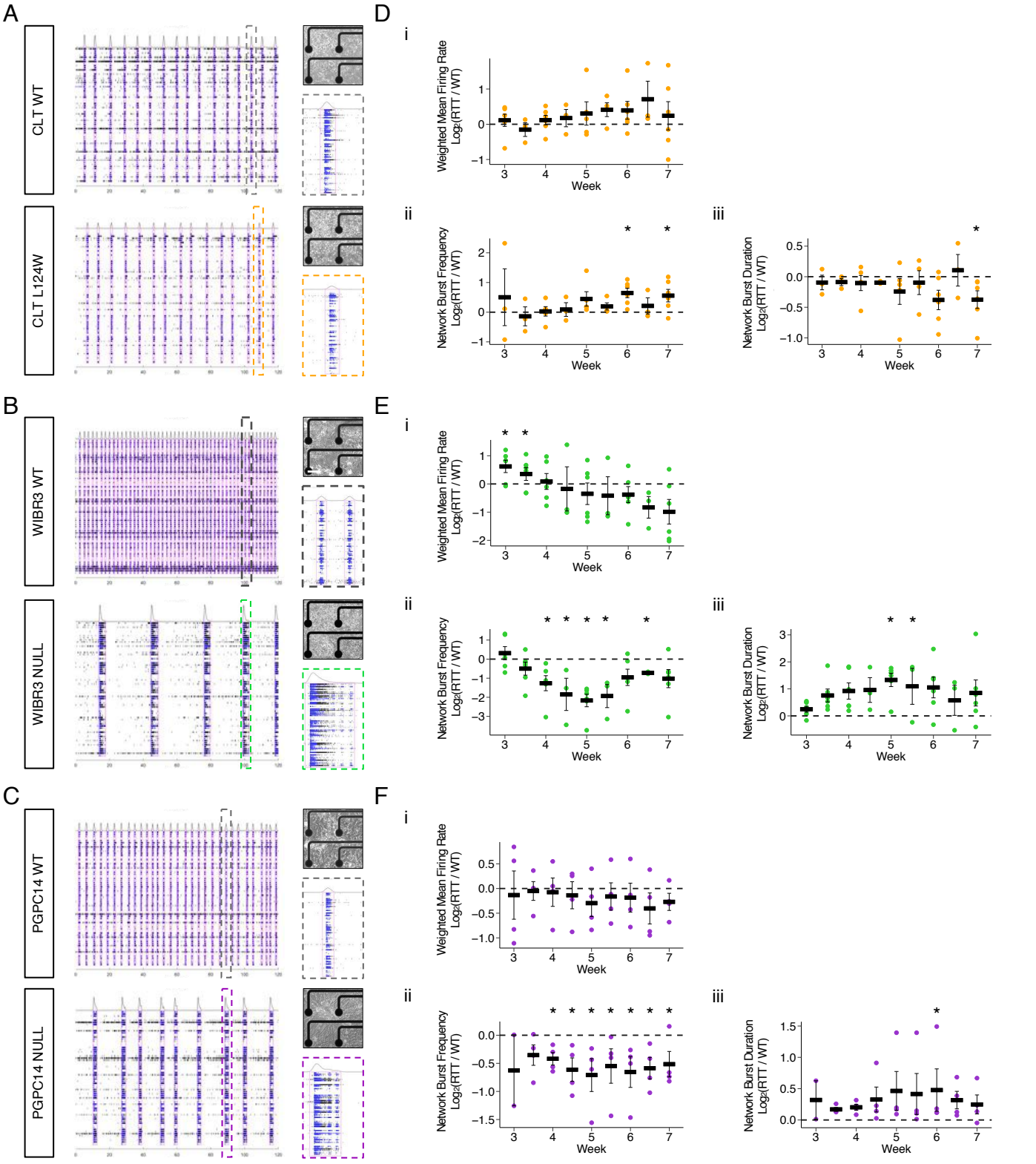
A
CLT WT
CLT L124W
B
WIBR3 WT
WIBR3 NULL
C
PGPC14 WT
PGPC14 NULL
D
E
F
i
ii
iii
Weighted Mean Firing Rate
Log2(RTT / WT)
Network Burst Frequency
Log2(RTT / WT)
Network Burst Duration
Log2(RTT / WT)
Week

Figure S1

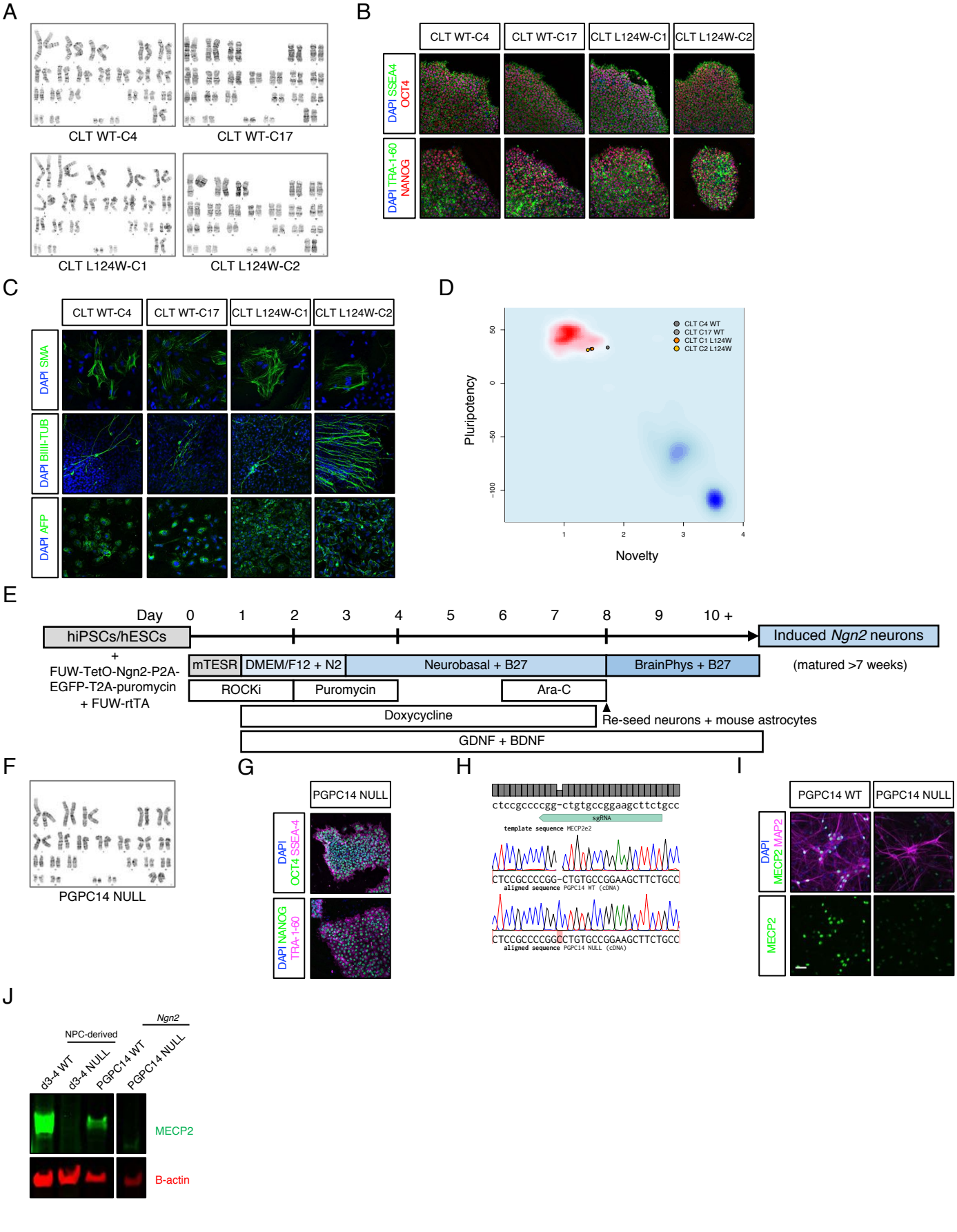
A
CLT WT-C4
CLT WT-C17
CLT L124W-C1
CLT L124W-C2
B
CLT WT-C4
CLT WT-C17
CLT L124W-C1
CLT L124W-C2
DAPI SSEA4 OCT4
DAPI TRA-1-60 NANOG
C
CLT WT-C4
CLT WT-C17
CLT L124W-C1
CLT L124W-C2
DAPI SMA
DAPI BIII-TUB
DAPI AFP
D
CLT C4 WT
CLT C17 WT
CLT C1 L124W
CLT C2 L124W
Pluripotency
Novelty
E
Day 0 1 2 3 4 5 6 7 8 9 10 +
hiPSCs/hESCs
+
FUW-TetO-Ngn2-P2A-EGFP-T2A-puromycin
+ FUW-rtTA
Induced Ngn2 neurons
(matured >7 weeks)
mTESR
DMEM/F12 + N2
Neurobasal + B27
BrainPhys + B27
ROCKi
Puromycin
Ara-C
Doxycycline
Re-seed neurons + mouse astrocytes
GDNF + BDNF
F
PGPC14 NULL
G
PGPC14 NULL
DAPI CCT4 SSEA-4
DAPI NANOG TRA-1-60
H
ctccgccccgg-ctgtgccggaagcttctgcc
sgRNA
template sequence MECP2e2
CTCCGCCCCGG-CTGTGCCGGAAGCTTCTGCC
aligned sequence PGPC14 WT (cDNA)
CTCCGCCCCGGCCTGTGCCGGAAGCTTCTGCC
aligned sequence PGPC14 NULL (cDNA)
I
PGPC14 WT
PGPC14 NULL
DAPI MECP2 MAP2
MECP2
J
Ngn2
NPC-derived
d3-4 WT
d3-4 NULL
PGPC14 WT
PGPC14 NULL
MECP2
B-actin

Figure S2

A

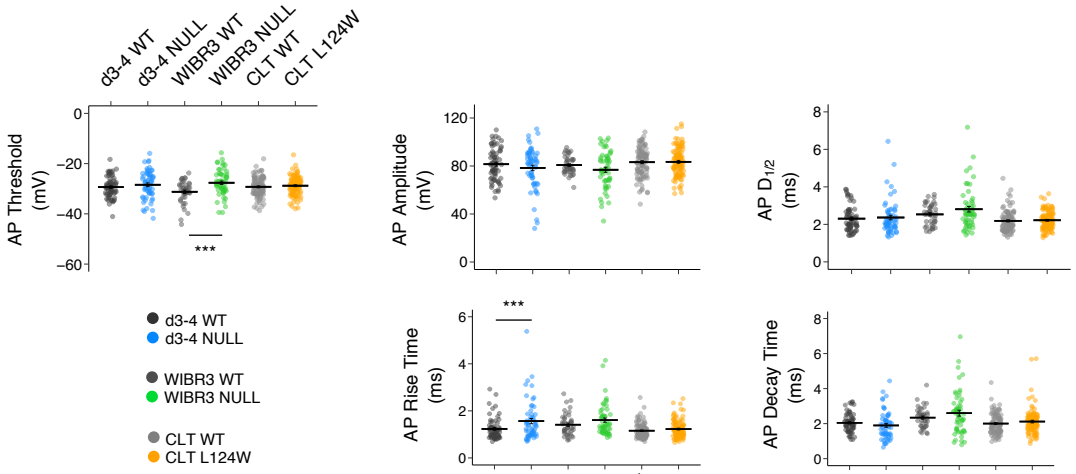

Figure S3

A

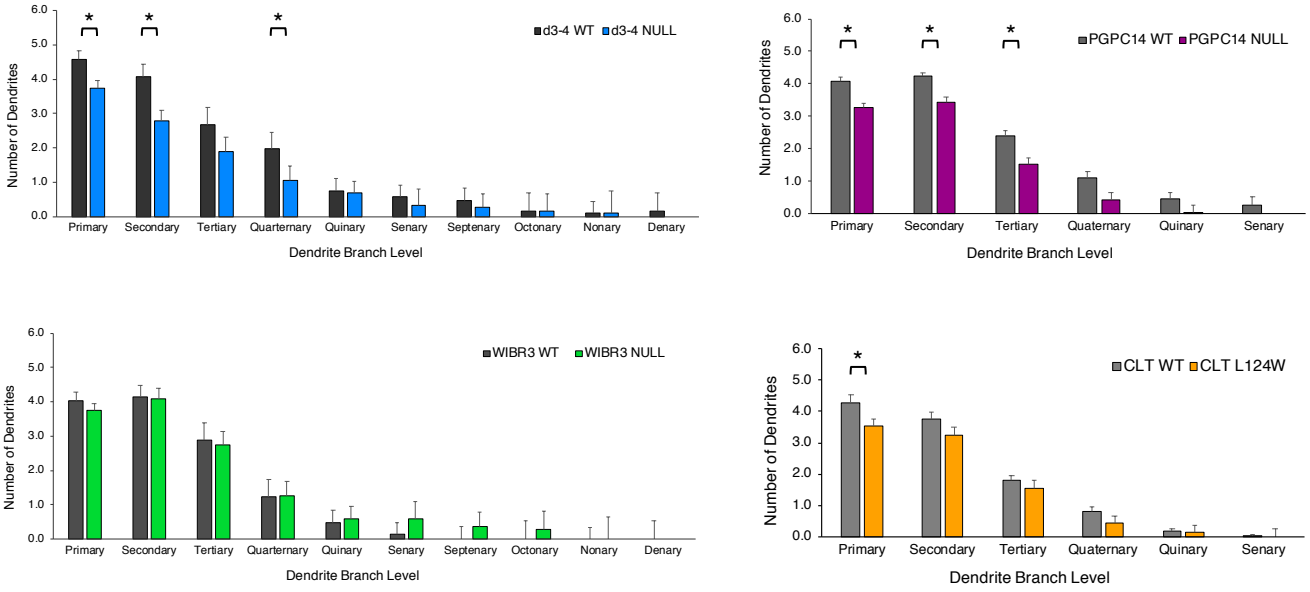

Figure S4

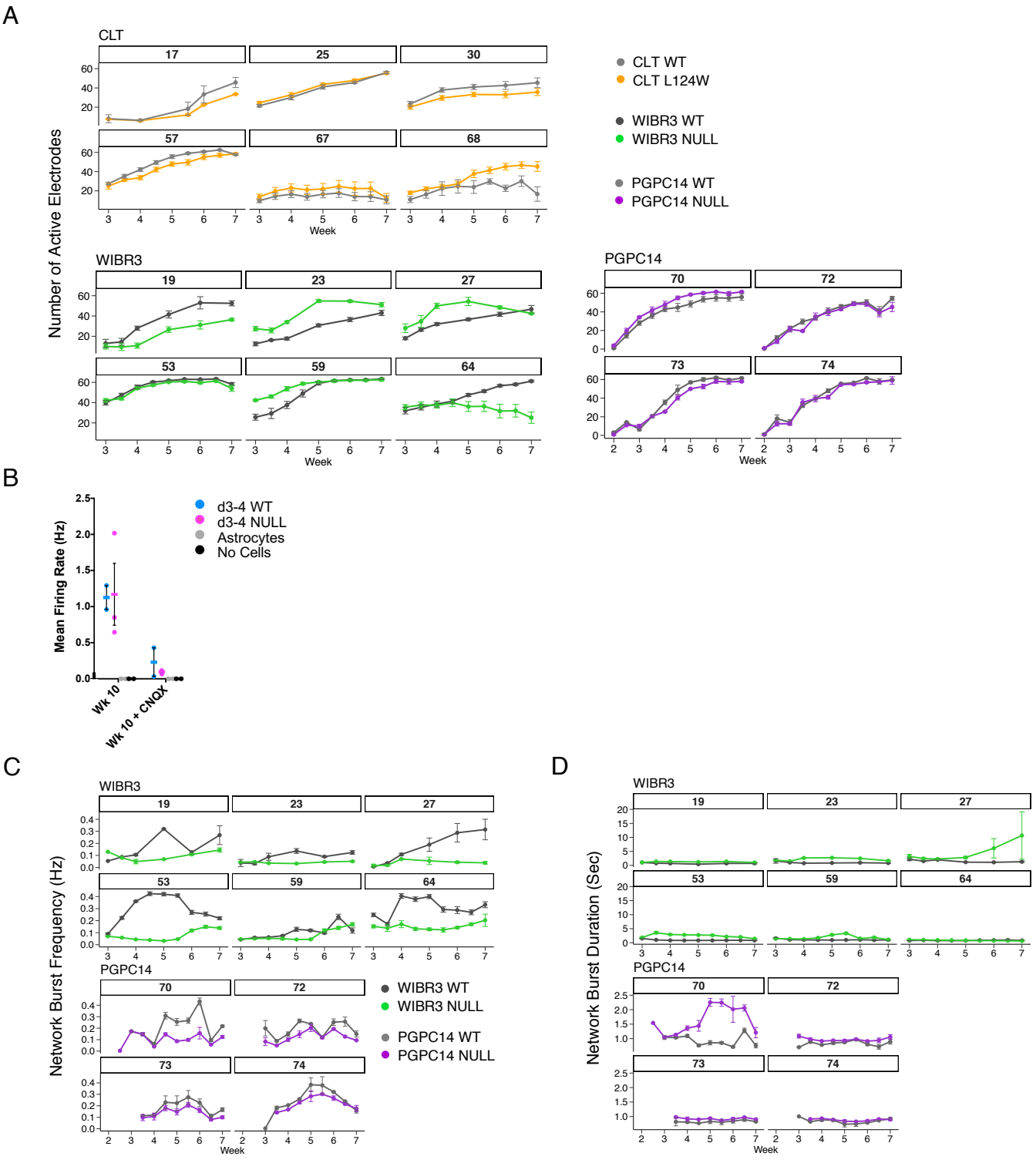
A
CLT
17
25
30
57
67
68
WIBR3
19
23
27
53
59
64
PGPC14
70
72
73
74
Number of Active Electrodes
Week
CLT WT
CLT L124W
WIBR3 WT
WIBR3 NULL
PGPC14 WT
PGPC14 NULL
B
Mean Firing Rate (Hz)
d3-4 WT
d3-4 NULL
Astrocytes
No Cells
Wk 10
Wk 10 + CNQX
C
Network Burst Frequency (Hz)
D
Network Burst Duration (Sec)